

## THE RELATIONSHIP BETWEEN GAS CONTENT AND STAR FORMATION IN MOLECULE-RICH SPIRAL GALAXIES

TONY WONG<sup>1</sup> AND LEO BLITZ

Astronomy Department and Radio Astronomy Laboratory, University of California, Berkeley, CA 94720

Received 2001 September 17; accepted 2001 December 5

### ABSTRACT

We investigate the relationship between H I, H<sub>2</sub>, and the star formation rate (SFR) using azimuthally averaged data for seven CO-bright spiral galaxies. Contrary to some earlier studies based on global fluxes, we find that  $\Sigma_{\text{SFR}}$  exhibits a much stronger correlation with  $\Sigma_{\text{H}_2}$  than with  $\Sigma_{\text{HI}}$ , as  $\Sigma_{\text{HI}}$  saturates at a value of  $\sim 10 \text{ M}_\odot \text{ pc}^{-2}$  or even declines for large  $\Sigma_{\text{SFR}}$ . Hence the good correlation between  $\Sigma_{\text{SFR}}$  and the total (H I+H<sub>2</sub>) gas surface density  $\Sigma_{\text{gas}}$  is driven by the molecular component in these galaxies, with the observed relation between  $\Sigma_{\text{SFR}}$  and  $\Sigma_{\text{H}_2}$  following a Schmidt-type law of index  $n_{\text{mol}} \approx 0.8$  if a uniform extinction correction is applied or  $n_{\text{mol}} \approx 1.4$  for a radially varying correction dependent on gas density. The corresponding Schmidt law indices for  $\Sigma_{\text{gas}}$  vs.  $\Sigma_{\text{SFR}}$  are 1.1 and 1.7 for the two extinction models, in rough agreement with previous studies of the disk-averaged star formation law. An alternative to the Schmidt law, in which the gas depletion timescale is proportional to the orbital timescale, is also consistent with the data if radially varying extinction corrections are applied. We find no clear evidence for a link between the gravitational instability parameter for the gas disk ( $Q_g$ ) and the SFR, and suggest that  $Q_g$  be considered a measure of the gas fraction. This implies that for a state of marginal gravitational stability to exist in galaxies with low gas fractions, it must be enforced by the stellar component. In regions where we have both H I and CO measurements, the ratio of H I to H<sub>2</sub> surface density scales with radius as roughly  $R^{1.5}$ , and we suggest that the balance between H I and H<sub>2</sub> is determined primarily by the midplane interstellar pressure. These results favor a “law” of star formation in quiescent disks in which the ambient pressure and metallicity control the formation of molecular clouds from H I, with star formation then occurring at a roughly constant rate per unit H<sub>2</sub> mass.

*Subject headings:* galaxies: evolution — galaxies: ISM — stars: formation

### 1. INTRODUCTION

Understanding the factors which control the star formation rate (SFR) is of fundamental importance to studies of the interstellar medium (ISM) and galaxy evolution. The most important factor, of course, is the availability of cold neutral gas, especially molecular gas. Over the past several decades, observations of the CO(1-0) line have established a clear link between star formation in the Galaxy and molecular gas (e.g., Loren et al. 1973), and even in environments where star formation is observed without CO emission, such as dwarf irregular galaxies, a plausible case can be made that molecular clouds are weak CO emitters due to low metal abundances (Wilson 1995; Taylor et al. 1998). On the other hand, Kennicutt (1989) has shown that the disk-averaged  $\Sigma_{\text{SFR}}$  is much better correlated with  $\Sigma_{\text{HI}}$  than with  $\Sigma_{\text{H}_2}$  inferred from CO observations, a surprising result given the very different radial profiles of H I and H<sub>α</sub> emission in galaxies. Similar conclusions have been reached by other studies based on global averages (Deharveng et al. 1994; Boselli 1994; Casoli et al. 1996). Thus, it is not obvious whether the H I or H<sub>2</sub> (as traced by CO) content will be a better predictor of the SFR on large scales. Kennicutt (1989) argues that it is the *total* (H I+H<sub>2</sub>) gas surface density which shows the best correlation with the SFR per unit area.

A quantitative prescription for the SFR has been provided by Kennicutt (1998a, hereafter K98), who finds that the total gas surface density, averaged over the optical

disk, is related to the SFR surface density by a Schmidt (1959) law,

$$\Sigma_{\text{SFR}} \propto (\Sigma_{\text{gas}})^n. \quad (1)$$

where  $n \approx 1.4$ . Kennicutt’s formulation of the star formation law has been widely applied in “semi-empirical” models of galaxy evolution (e.g., Boissier & Prantzos 1999; Tan et al. 1999; van den Bosch & Dalcanton 2000). While the Schmidt law appears to be valid at high gas surface densities, Kennicutt (1989) and Martin & Kennicutt (2001) have presented evidence for a threshold density for star formation based on the gravitational instability parameter  $Q$ . Below the threshold density, which observationally is of order  $5-10 \text{ M}_\odot \text{ pc}^{-2}$ , the Schmidt law breaks down and star formation is strongly suppressed. The general applicability of a  $Q$  threshold, however, remains controversial (Thornley & Wilson 1995; Hunter et al. 1998; Ferguson et al. 1998).

As noted by K98, an alternative formulation of the star formation law, where the star formation timescale is proportional to the orbital timescale,

$$\Sigma_{\text{SFR}} \propto \Sigma_{\text{gas}} \Omega, \quad (2)$$

is also consistent with the disk-averaged data. Such a law is predicted by models in which spiral arms play an important role in triggering star formation (Wyse & Silk 1989), or in which star formation is self-regulated to yield a constant value of  $Q$  (Larson 1988; Silk 1997). Distinguishing between this law and a Schmidt law requires *spatially re-*

<sup>1</sup> Present address: CSIRO Australia Telescope National Facility, PO Box 76, Epping NSW 1710, Australia; Tony.Wong@csiro.au

solved measurements of gas densities and orbital timescales (i.e., rotation curves).

A third prescription for the SFR, arising from CO studies by J. Young and collaborators (Devereux & Young 1991; Young et al. 1996; Rownd & Young 1999), states that the SFR is roughly proportional to the mass of molecular gas, so that their ratio (commonly referred to as the *star formation efficiency*, SFE) is roughly constant. In particular, Rownd & Young (1999) find that the SFE within the disks of spiral galaxies exhibits no strong radial gradients, under the assumption of a constant CO-to-H<sub>2</sub> conversion factor. An SFE that is independent of galactocentric radius is also consistent with studies of molecular clouds in our Galaxy (Mead et al. 1990; Wouterloot et al. 1988). If star formation in disk galaxies can be generically decomposed into two processes, the formation of giant molecular clouds (GMCs) from H I clouds and the formation of stars within GMCs (e.g., Tacconi & Young 1986), then the latter process occurs at a rate that is largely independent of location within a galaxy, and may well be universal in all disk galaxies.

Previous studies of the star formation law in external galaxies have tended to concentrate on large samples observed at the low resolution provided by single-dish radio telescopes. Although such samples are valuable for characterizing the global properties of galaxies, detailed study of individual objects at high spatial resolution is essential for understanding the physical basis of the star formation law and reconciling the various empirical descriptions. In this paper we undertake such an investigation, comparing recent CO data from the BIMA Survey of Nearby Galaxies (BIMA SONG) with previously published H I and H $\alpha$  data. Our high-resolution CO maps include single-dish data, which is essential when accurate flux measurements are required for extended sources. We employ azimuthally

averaged radial profiles in order to improve the signal-to-noise ratio and average over time-dependent effects.

The organization of this paper is as follows. In §2 we describe our galaxy sample, observing parameters, and data reduction procedures. §3 describes how we produced radial profiles from the intensity images and our corrections for H $\alpha$  extinction. §4.1 presents our results for the relation between  $\Sigma_{\text{SFR}}$  and  $\Sigma_{\text{gas}}$ , as well as the relations between  $\Sigma_{\text{SFR}}$  and  $\Sigma_{\text{HI}}$  and  $\Sigma_{\text{H}_2}$  individually. In §4.2 we compare  $\Sigma_{\text{gas}}$  with the threshold surface density discussed by Kennicutt (1989), and in §4.3 we investigate the relationship between the radial profiles of atomic and molecular gas. In §5 we show how our results can be interpreted in terms of a nearly constant star formation efficiency for molecular gas, with molecular cloud formation in turn linked to the average ISM pressure. Finally, in §6 we summarize our results. In subsequent papers of this series, we will analyze the CO and H I kinematics of the galaxies in our sample for evidence of radial inflows (Wong, Blitz, & Bosma 2002, Paper II) and evaluate whether the observed gas depletion times and oxygen abundances are consistent with closed-box evolution (Wong & Blitz 2002, Paper III).

## 2. OBSERVATIONS AND DATA REDUCTION

### 2.1. Sample Description

Most of the new observations presented in this paper were taken as part of the BIMA Survey of Nearby Galaxies (BIMA SONG) (Regan et al. 2001), an interferometric CO survey of 44 spiral galaxies selected primarily by optical luminosity (absolute  $B$  magnitude  $M_B < 11$ ). Six of these galaxies, along with NGC 4501, were chosen for this study. All exhibit strong CO emission at a range of radii and have available H I maps from the Very Large Array (VLA) at the resolution of the C configuration ( $\sim 20''$ )

TABLE 1  
PROPERTIES OF THE SAMPLE GALAXIES

Name	RA (2000) hh:mm:ss	DEC dd:mm:ss	Morph. Type	$B_T^0$ <sup>(a)</sup> (mag)	$R_{25}$ <sup>(b)</sup> (arcsec)	$V_{\odot}$ <sup>(c)</sup> (km/s)	Dist. (Mpc)
NGC 4321	12:22:54.9	15:49:21	SAB(s)bc	9.98	220	1571	16 <sup>(d)</sup>
NGC 4414	12:26:27.1	31:13:24	SA(rs)c?	10.62	110	716	19 <sup>(e)</sup>
NGC 4501	12:31:59.2	14:25:14	SA(rs)b	9.86	210	2281	16 <sup>(d)</sup>
NGC 4736	12:50:53.1	41:07:14	(R)SA(r)ab	8.75	340	308	4.2 <sup>(f)</sup>
NGC 5033	13:13:27.5	36:35:38	SA(s)c	10.21	320	875	17.5 <sup>(g)</sup>
NGC 5055	13:15:49.3	42:01:45	SA(rs)bc	9.03	380	504	10 <sup>(g)</sup>
NGC 5457	14:03:12.5	54:20:55	SAB(rs)cd	8.21	870	241	7.4 <sup>(h)</sup>

<sup>a</sup>Total blue magnitude, corrected for Galactic and internal absorption and redshift, from RC3 (de Vaucouleurs et al. 1991).

<sup>b</sup>Semimajor axis at 25.0 mag arcsec<sup>-2</sup>, from RC3.

<sup>c</sup>Heliocentric velocity, from NED.

<sup>d</sup>Cepheid distance to NGC 4321 from Ferrarese et al. (1996) adopted for Virgo cluster.

<sup>e</sup>Cepheid distance from Turner et al. (1998).

<sup>f</sup>Redshift distance using  $H_0 = 75$  km s<sup>-1</sup> Mpc<sup>-1</sup>.

<sup>g</sup>Distance from Mark III data (Willick et al. 1997) using  $H_0=75$ .

<sup>h</sup>Cepheid distance from Kelson et al. (1996).

or better. The insistence on high-resolution H I data is essential for the CO and H I data to be used in a complementary way; although H I maps at even higher ( $\sim 6''$ ) resolution would be ideal, few such maps are available because of the large investment of observing time needed to obtain good sensitivity at those resolutions. The galaxies span a range of morphological type, from Sab to Scd. While none are involved in strong interactions with other galaxies, NGC 4321 (M100) and NGC 4501 are members of the Virgo Cluster and presumably interacting with the intracluster medium. The basic properties of the sample are summarized in Table 1. The tabulated coordinates are for the center of the galaxy as given by the NASA Extragalactic Database (NED), except for NGC 5055 where we have adopted the peak of the astrometrized  $K$ -band image of Thornley & Mundy (1997a).

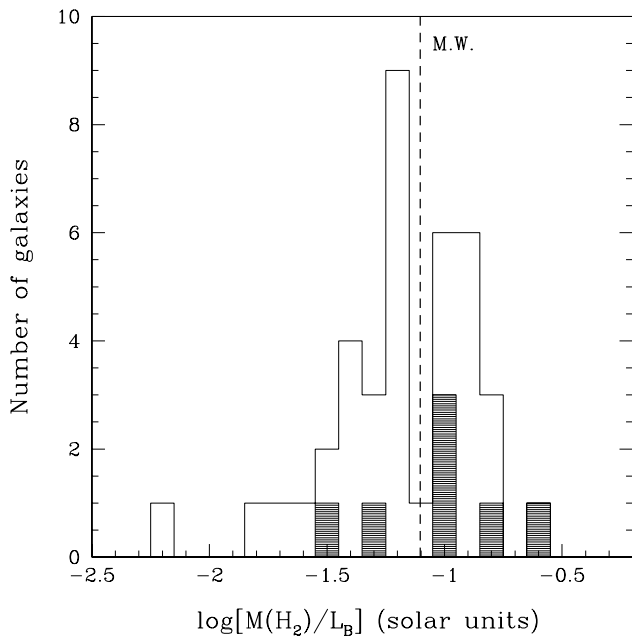


FIG. 1.— Histogram of  $H_2$  masses normalized by  $B$  luminosity, using data from Young et al. (1995) and a constant  $X$ -factor, for our sample (shaded) and 40 of the 44 galaxies in the optically selected BIMA SONG sample. The remaining 4 galaxies were not observed by Young et al. (1995) and probably have below-average CO fluxes. For NGC 5457 (second shaded box from left) we have used the CO flux measured by Kenney et al. (1991), which is probably an underestimate since their map is incomplete. The vertical dashed line is for the Milky Way.

Based on single-dish measurements from the Five College Radio Astronomy Observatory (FCRAO) Extragalactic CO Survey (Young et al. 1995), the median CO flux for the galaxies in our sample is  $2760 \text{ Jy km s}^{-1}$ , compared to a median of  $1640 \text{ Jy km s}^{-1}$  for the entire SONG sample. To determine if the difference results from our choice of more optically luminous galaxies, Figure 1 shows a histogram of the ratio of  $H_2$  mass to  $B$ -band luminosity as tabulated by Young et al. (1995), for the galaxies in our sample (shaded) as well as for the entire SONG sample. We have scaled the CO fluxes derived by Young et al. (1995) to  $H_2$  masses using a conversion factor appropriate

for the Galaxy:

$$N_{H_2} = 2 \times 10^{20} \left( \frac{I_{CO}}{\text{K km s}^{-1}} \right) \text{ cm}^{-2}, \quad (3)$$

(Strong & Mattox 1996; Dame et al. 2001). The median for the entire SONG sample ( $-1.17$  dex in solar units) is somewhat less than the value for the Milky Way ( $-1.1$  dex, based on Dame 1993 and van der Kruit 1990), which in turn is less than the median for our sample ( $-1.0$  dex). Note that a difference of 0.17 dex corresponds to a factor of 1.5. Despite considerable uncertainty in the FCRAO fluxes, since they are estimated from major axis scans rather than complete two-dimensional maps, we conclude that the galaxies in our sample are somewhat overluminous in CO (relative to their optical luminosities) compared to bright galaxies in general. This is not surprising, given that we explicitly required that CO be observed over a large portion of the galaxy disk. Thus, one should bear in mind that properties of the ISM in the galaxies studied here may not be representative of the field galaxy population, or even the population of optically luminous galaxies.

## 2.2. BIMA CO Observations

Observations with the BIMA<sup>2</sup> interferometer at Hat Creek, California were conducted primarily in the C array configuration, which gives a synthesized beam of  $\sim 6''$  FWHM, with a few additional observations (“tracks”) taken in the D array configuration ( $15''$  FWHM). The synthesized beam gives the resolution of the resulting maps, and is determined by the maximum spacing of the antennas: in C-array the spacings range from 7 to 90 m (2.7–35  $k\lambda$ ), while in D-array the spacings range from 7 to 30 m (2.7–11  $k\lambda$ ). Several of the C-array observations of NGC 4501, 4736, and 5033 were made in 1996 and 1997 when the BIMA array consisted of nine antennas; all other observations were made in 1998 and 1999 with ten antennas.

In our standard frequency setup, the receivers were tuned to the CO ( $J = 1 \rightarrow 0$ ) transition at 115.2712 GHz ( $\lambda=2.6 \text{ mm}$ ), with the correlator configured to have 4 independently positioned spectral windows, each with 100 MHz bandwidth and 64 channels. The spectral windows were placed side-by-side in frequency with an overlap of  $\approx 10 \text{ MHz}$  (6 channels). The resulting velocity range covered was  $\approx 950 \text{ km s}^{-1}$  at a resolution of  $4.06 \text{ km s}^{-1}$ . Data from the lower sideband of the first local oscillator, at a frequency of 112 GHz, were also recorded, but no continuum emission was detected in any of the sample galaxies.

At  $\lambda=2.6 \text{ mm}$  the BIMA antennas have a primary beam FWHM of  $100''$ , which defines the effective field of view. During most observing sessions a 7-point hexagonal grid centered on the galaxy nucleus was observed, with the points separated by  $50''$  (for NGC 4501 and 4736) or  $44''$  (for the remaining galaxies). In order to maintain roughly equal sampling in the visibility plane for each pointing center, the entire grid was observed in 7–9 minutes and then repeated. For a few tracks on NGC 4414, 4736, and 5033, only the central pointing was observed. In cases where the same galaxy was observed as both a single pointing and a mosaic, the tracks were imaged together as a mosaic—with the exception of NGC 4414, where only the central pointing was used for the high-resolution map. The resulting values of  $R_{\max}$  for each datacube, defined as the radius at

<sup>2</sup> The Berkeley-Illinois-Maryland Association is funded in part by the National Science Foundation.

TABLE 2  
PROPERTIES OF THE BIMA CO MAPS

Galaxy	Weighting	Resolution ( $'' \times '' \times \text{km s}^{-1}$ )	PA <sup>(a)</sup> ( $^{\circ}$ )	$\sigma_{ch}^{(b)}$ (mJy/bm)	$R_{\max}^{(c)}$ ( $''$ )
NGC 4321	natural	$8.85 \times 5.62 \times 10$	4.7	49	94
	20'' taper	$20 \times 20 \times 10$	0.0	97	
NGC 4414	robust	$6.53 \times 4.88 \times 10$	8.2	42	50
	13'' taper	$17.5 \times 15.3 \times 10$	72.1	64	94
NGC 4501	natural	$7.89 \times 6.23 \times 20$	-80.9	56	100
	22'' taper	$23.2 \times 22.3 \times 10$	24.6	174	
NGC 4736	robust	$6.86 \times 5.02 \times 10$	62.5	69	100
	13'' taper	$15 \times 15 \times 10$	0.0	83	
NGC 5033	natural	$7.52 \times 6.49 \times 20$	82.8	52	94
	18'' taper	$19.9 \times 17.0 \times 20$	89.1	108	
NGC 5055	robust	$5.69 \times 5.30 \times 10$	13.9	83	94
	12'' taper	$12.9 \times 12.8 \times 10$	-83.5	107	
NGC 5457	natural	$6.88 \times 6.36 \times 10$	72.5	43	94
	15'' taper	$15 \times 15 \times 10$	0.0	80	

<sup>a</sup>Position angle of beam measured from N towards E.

<sup>b</sup>RMS noise in a single emission-free channel measured across the inner  $2' \times 2'$ , in mJy  $\text{bm}^{-1}$ .

<sup>c</sup>Radius at which half-power point of the outermost pointing is reached.

which one reaches the half-power point of the outermost pointing, are given in Table 2.

### 2.2.1. Assessment of Data Quality

The two principal factors which can affect the data quality from a millimeter-wave interferometer are the tropospheric water vapor column, which increases the atmospheric opacity, and fluctuations in that column, which lead to variations in the refractive index of the atmosphere (“seeing”) and hence variations in the phase of the signal measured at the telescope. Changes in atmospheric opacity are reflected in the “effective” system temperature  $T_{\text{sys}}^*$ , which ranged from 300–600 K during our observations, depending on the source elevation and weather conditions. Atmospheric phase noise can be quantified by a frequency-independent quantity  $\sigma_{\text{path}}$ , representing the RMS fluctuation in the difference in effective path length through the atmosphere for two parallel sight lines separated by a given distance (e.g., Wright 1996). Since mid-1998,  $\sigma_{\text{path}}$  has been measured every 10 minutes at Hat Creek by a dedicated phase monitor, which records signals from a television satellite using a pair of commercial satellite dishes separated by 100 m (Lay 1999). These measurements yield a fiducial  $\sigma_{\text{path},0}$ , which was typically 200–400  $\mu\text{m}$  for the C-array observations and 800–1200  $\mu\text{m}$  for the D-array observations (the latter occurring mostly in summer). Note that with the RMS phase given by  $\phi_{\text{rms}} = 2\pi\sigma_{\text{path}}/\lambda$ , the visibility amplitude after time-averaging is given by

$$\langle V \rangle = V_0 e^{-(\phi_{\text{rms}})^2/2}. \quad (4)$$

Hence a value of  $\sigma_{\text{path},0} = 560 \mu\text{m}$  corresponds to a 50% decorrelation (i.e. loss of visibility amplitude) at  $\lambda = 3 \text{ mm}$  for a 100 m baseline (Akeson 1998), roughly the

longest baseline in the C-array. Although the measured  $\sigma_{\text{path},0}$  was typically worse than this in D-array, the actual phase fluctuations that affect the short baselines of D-array ( $b \ll 100 \text{ m}$ ) are much smaller since  $\sigma_{\text{path}} \propto b^{5/6}$  (Wright 1996).

### 2.2.2. Data Calibration

The data were calibrated and reduced following the procedures described in Regan et al. (2001). We give only a summary here. An online linelength calibration was applied to correct for variations in the electrical path length from the antenna to the correlator. Remaining drifts in the antenna phase gains were then corrected by observing a nearby (within  $\sim 15^{\circ}$ ) quasar every half hour and fitting a low-order (quadratic or cubic) polynomial to the antenna-based self-calibration solutions. Mars was used for amplitude calibration except in 1998 April, when the quasar 3C273 was used. For all tracks both amplitude and phase gains were assumed to be frequency-independent; this approximation was found to be adequate in several cases by observing 3C273 using the same correlator setup as for the source observations.

For tracks during which  $\sigma_{\text{path}}$  was measured, an additional calibration step was performed in order to compensate for the effects of phase decorrelation on the maps. In this procedure, implemented in a MIRIAD task called UVDECOR written by M. Regan, the visibility amplitudes for all datasets are scaled up by a baseline-dependent correction factor, typically  $\sim 1$ –1.2, based on the expected amplitude loss due to phase decorrelation (see Regan et al. 2001). We found that applying UVDECOR led to a  $\sim 10\%$  increase in the fluxes of the final maps. Overall, we estimate that the flux scale of the resulting BIMA maps is

accurate to within  $\sim 20\%$ .

Following the initial calibration, the visibilities were subjected to three iterations of phase-only self-calibration, which in all cases led to convergence. Channel maps were then produced for each galaxy by assigning weights to the calibrated visibilities as described below, transforming to the image plane after binning to 10 or 20  $\text{km s}^{-1}$  channels (to improve signal-to-noise), and deconvolving using a variant of the CLEAN algorithm developed by Steer et al. (1984) to improve the deconvolution of spatially extended emission. In general, assigning greater weight to short-baseline data results in lower resolution but higher signal-to-noise for extended sources, as well as reduced systematic errors because short baselines are less subject to atmospheric phase noise. Thus, for all galaxies we generated a low-resolution map by applying a Gaussian taper in the visibility plane, chosen to match the resolution of the galaxy's H I cube. In addition, a high-resolution map was generated using either natural or robust weighting. Natural weighting provides the best point-source sensitivity and was used for sources with poorer signal-to-noise (NGC 4321, 4501, 5033, and 5457). Robust weighting, which provides poorer sensitivity but somewhat higher resolution, was used for NGC 4414, 4736, and 5055. Table 2 summarizes the properties of the final deconvolved maps.

### 2.3. Kitt Peak CO Observations

Single-dish CO observations were performed at the NRAO<sup>3</sup> 12m telescope on Kitt Peak, Arizona. We refer to these data hereafter as the "KP data." At  $\lambda=2.6$  mm the half-power beamwidth (HPBW) of the telescope is  $55''$ . All galaxies with the exception of NGC 4501 were observed between 1998 April and 2000 January using the On-The-Fly (OTF) technique, in which the telescope is scanned rapidly across the sky and spectra are written out at a very high rate (every 0.1 s). The relative pointing of the telescope during the map is also continuously measured, although the absolute pointing must still be checked and adjusted at regular intervals (once every 1–2 hr) by observing a bright continuum source (typically Mars). Each map covered a field roughly  $6' \times 6'$  in size and was completed in  $\lesssim 15$  minutes; roughly 20–40 maps were obtained per galaxy and later co-added during data reduction. NGC 4501 was observed in 1997 June in position-switched (hereafter PS) mode, where spectra are taken at specified grid points spaced by half a beamwidth or less. The integration time was typically 4–8 minutes per pointing, with a total of 27 pointings observed covering a region roughly  $2' \times 2'$  in size.

The telescope was configured to observe orthogonal polarizations using two 256-channel filterbanks (one for each polarization) at a spectral resolution of 2 MHz (5.2  $\text{km s}^{-1}$ ). Calibration was performed using the chopper wheel method every 5–15 minutes; typical values of  $T_{\text{sys}}^*$  were 300–400 K. Spectra were output on the  $T_R^*$  scale, which represents the source antenna temperature corrected for ohmic losses, atmospheric absorption, spillover, and scattering (Kutner & Ulich 1981). Background emission was measured by observing an off-source position  $10'$  from the pointing center (for the PS observations) or by

averaging spectra at the edges of the OTF maps; the off-source spectrum nearest in time was then used for background subtraction.

Data reduction was performed in the COMB software package for the PS spectra and the AIPS and MIRIAD packages for the OTF spectra. A linear baseline was fitted to the signal-free channels of each spectrum and subtracted. FITS datacubes were then generated using a cell size of  $13.5''$  for the PS map and  $18''$  for the OTF maps. For each galaxy, the RMS noise in the final maps ranged from 14–28 mK in a 2 MHz channel. The maps were converted into Jy units using a standard telescope gain of  $33 \text{ Jy (K[T}_R^{\text{]})}^{-1}$ .

Prior to combination with the BIMA maps, OTF maps from different dates were cross-correlated against each other to correct for pointing offsets, as described in Regan et al. (2001). The derived offsets were generally around  $10''$  but ranged as high as  $27''$  (half a beam width) in one case. After this internal registration of the OTF maps, a final cross-correlation with the BIMA map (smoothed to  $55''$ ) was performed, under the assumption that the flux resolved out by BIMA did not significantly affect the centroid of the CO emission. The resulting corrections amounted to  $5''$ – $11''$ . For NGC 5457, which has a low inclination and a large angular diameter, this assumption was found to be inappropriate due to the large amount of flux missing from the BIMA map, and the final cross-correlation was not performed.

### 2.4. CO Data Combination

The relative calibration between two millimeter telescopes is always somewhat uncertain, so when combining single-dish and array data one typically attempts to solve for a relative calibration factor, using data from both telescopes that have been filtered to the same range of spatial frequencies. The factor needed to scale the KP data to match the BIMA data was calculated for each galaxy using the MIRIAD task IMMERGE and ranged from 1 to 1.3. In the case of NGC 4501, a reliable calibration factor could not be determined since the field of view of the KP observations was not large enough, so a factor of 1 was adopted. We note that it is quite possible that the BIMA data should be scaled down rather than the KP data scaled up; this is especially likely if the effect of decorrelation has been overestimated when applying UVDECOR. For simplicity, we assume here that the BIMA data have the "correct" flux scale and emphasize that the CO fluxes we measure may be slightly overestimated. Given the uncertainties in converting CO brightness to H<sub>2</sub> column density, an overall scaling factor of  $\lesssim 1.3$  is probably unimportant.

We examined two methods of combining the BIMA and KP data, one which generates a weighted sum of the two cubes before deconvolution (the "dirty-map" combination method) and another which folds in the KP data after the BIMA map has been deconvolved, by partially replacing the inner part of the Fourier plane with the KP data. The two methods gave similar results to within the noise. We adopted the latter method, as implemented in the IMMERGE task. The resulting datacubes are sensitive to structures on all spatial scales larger than  $\sim 6''$ . A more

<sup>3</sup> The National Radio Astronomy Observatory is a facility of the National Science Foundation, operated under cooperative agreement by Associated Universities, Inc.

TABLE 3  
PROPERTIES OF THE VLA HI MAPS

Galaxy	Resolution ( $'' \times '' \times \text{km s}^{-1}$ )	PA <sup>(a)</sup> ( $^{\circ}$ )	$\sigma_{ch}^{(b)}$ (mJy/bm)	Reference
NGC 4321	$20 \times 20 \times 20.6$	0.0	0.75	Knapen et al. (1993)
NGC 4414	$17.5 \times 15.3 \times 10.3$	72.1	0.4	Thornley & Mundy (1997b)
NGC 4501	$23.2 \times 22.3 \times 10.3$	24.6	0.6	A. Bosma (Paper II)
NGC 4736	$15 \times 15 \times 5.15$	0.0	1.8	Braun (1995)
NGC 5033	$19.9 \times 17.0 \times 20.6$	89.1	0.3	Thean et al. (1997)
NGC 5055	$12.9 \times 12.8 \times 10.3$	-83.5	0.2	Thornley & Mundy (1997a)
NGC 5457	$15 \times 15 \times 5.15$	0.0	1.8	Braun (1995)

<sup>a</sup>Position angle of beam measured from N towards E.

<sup>b</sup>RMS noise in a single emission-free channel measured across the inner  $4' \times 4'$ , in mJy  $\text{bm}^{-1}$ .

detailed discussion of issues surrounding the combination of single-dish and interferometer data can be found in Appendix B of Wong (2000).

### 2.5. HI Data

The H I data used in this study were obtained at the NRAO Very Large Array (VLA) by other researchers, who kindly provided us with reduced datacubes in FITS format. The properties of these cubes and references to the original papers in which they were presented are given in Table 3. (Details of the NGC 4501 observations will be presented in Paper II.) At  $\lambda=21$  cm the HPBW of the VLA is  $32'$ . All galaxies were observed in the C configuration, which gives a synthesized beam of  $\sim 13''$  for uniform weighting and  $\sim 20''$  for natural weighting; three of the galaxies (NGC 4736, 5055, and 5457) were also observed at higher resolution in the B configuration. Data obtained in the D configuration are included for all galaxies except NGC 4501 and 5033, so that the resulting maps are sensitive to even very extended ( $\sim 10'$ ) emission. The datacubes were imported into MIRIAD and transformed

to the spatial and velocity coordinate frames of the BIMA cubes.

### 2.6. $\text{H}\alpha$ Images

Continuum-subtracted  $\text{H}\alpha + [\text{N II}]$  CCD images were obtained from a variety of sources, as listed in Table 4. All images were originally taken at the Kitt Peak National Observatory (KPNO) 0.9-m telescope, except for NGC 5033 (Palomar 60-inch) and 5457 (KPNO Burrell Schmidt telescope). For NGC 4321 and 5055, the images were obtained in 1999 April under photometric conditions, with the standard stars Feige 34 and PG 0939+262 used for flux calibration (Massey et al. 1988). The other images have not been flux calibrated, so the flux scale was determined by comparison with published  $\text{H}\alpha$  fluxes in the literature, as stated in the table. Note that the fluxes of Kennicutt & Kent (1983) have been scaled up by a correction factor of 1.16 (K98). The uncertainty in our bootstrap calibration is at least as large as the uncertainty in the original published fluxes (generally  $\sim 25\%$ ). However, this will only affect the overall flux level, which is subject to significant

TABLE 4  
SOURCES FOR  $\text{H}\alpha$  IMAGES

Galaxy	Image Size	$-\log f_{\text{H}\alpha}^{(a)}$	Credit	Photometry Reference
NGC 4321	$11'$	11.28	M. Regan, K. Sheth	Massey et al. (1988)
NGC 4414	$11'$	11.38	Thornley & Mundy (1997b)	Thornley & Mundy (1997b)
NGC 4501	$6'$	11.14	Martin & Kennicutt (2001)	Young et al. (1996)
NGC 4736	$6'$	10.80	Martin & Kennicutt (2001)	Kennicutt & Kent (1983)
NGC 5033	$12'$	11.29	M. Regan	Kennicutt & Kent (1983)
NGC 5055	$11'$	10.74	M. Regan, K. Sheth	Massey et al. (1988)
NGC 5457	$20'$	10.18	van Zee et al. (1998)	Kennicutt (1988)

<sup>a</sup> $f_{\text{H}\alpha}$  is the total flux in the image, given in  $\text{erg cm}^{-2} \text{s}^{-1}$ .

uncertainties anyway when converted into a star formation rate (§3.2.3).

Since most of the images contained artifacts due to bad pixels, cosmic ray events, and foreground stars that were not cleanly subtracted (e.g., due to changes in seeing), these were masked out interactively using the IRAF task IMEDIT. Artifacts isolated from emission were replaced with zero values, while those superposed on diffuse emission were replaced by a background substitution algorithm that fits a smooth surface to an annular region of the image centered on the artifact. Remaining outliers were removed by clipping negative values below  $-5\sigma$  and positive values above a limit determined by visually identifying the brightest H II region. Astrometry was performed by comparing the locations of stars in the continuum image with a DSS image using the KARMA package (Gooch 1995) and then transferring the plate solution to the H $\alpha$  image; in some cases there were compact H $\alpha$  sources visible in the DSS image and the astrometry could be determined by direct comparison to the H $\alpha$  image. Astrometric errors should be less than 2''.

### 3. DATA ANALYSIS

#### 3.1. Intensity Images

Integrated intensity (“moment-0”) images were produced from the CO and H I datacubes using a masking technique designed to exclude noise. The necessity for such a procedure arises from the fact that the emission at any given pixel is usually confined to a small range of velocities, so a direct sum of all channels in the datacube would result in very poor signal-to-noise (see discussion in Bosma 1981; van der Kruit & Shostak 1982). Thus, employing a similar technique to Braun (1995), we defined a search region in each channel map by the  $3\sigma_{\text{smo}}$  contour of a smoothed version of the map, and included pixels within that region with intensities  $|I| > \sigma_{\text{ch}}$  in the sum (here  $\sigma_{\text{smo}}$  and  $\sigma_{\text{ch}}$  are the RMS noise per channel in the smoothed and original cubes respectively). Tests showed that while use of this masking technique does not have a significant effect on the total flux in the datacube, it does improve the accuracy with which weaker emission features are represented.

The resulting intensity images are displayed in Figure 2. For each galaxy, the top panels show the CO intensity map at full resolution and the corresponding H $\alpha$  image for comparison. The field of view of the BIMA mosaic (where the sensitivity drops to half of its peak value) is shown as a dotted contour. Most galaxies show a strong correspondence between CO and H $\alpha$  emission, although the emission peaks do not always coincide. In this respect, NGC 4736 appears unusual since the CO and H $\alpha$  distributions show fundamentally different symmetries, as discussed in Wong & Blitz (2000). With the exception of NGC 4736 and 5033, the CO emission appears to extend to the edge of the observed field, suggesting that our observations sample only the inner part of the molecular disk. (At a mean distance of 13 Mpc, our CO observations extend to  $R \approx 6.3$  kpc.)

The bottom panels for each galaxy show the tapered CO intensity map alongside the VLA H I intensity map. Both maps have the same spatial resolution (indicated by the beam in the lower left corner of each panel). We find that four of the galaxies (NGC 4321, 4501, 4736, 5457)

show both an H I deficit and CO enhancement in their inner regions, suggesting a large-scale conversion of atomic to molecular gas. This phenomenon has long been noted (e.g., Morris & Lo 1978), and its occurrence appears to be unrelated to the Hubble type of the galaxy, since 4736 is classified as early-type (Sab) whereas 5457 is classified as late-type (Scd).

#### 3.2. Radial Profiles

Radial profiles were derived from the intensity images by averaging in elliptical annuli spaced by roughly half the synthesized beamwidth and centered on the position given in Table 1. The annuli were assumed to be circular rings viewed at an inclination  $i$  and with a line of nodes rotated from north to east by some position angle (PA); the adopted values of PA and  $i$  for each galaxy are given in Table 5. As described in Paper II, the appropriate PA for each galaxy was determined by kinematic fits to the velocity field, while  $i$  was determined from isophotal and/or kinematic fits. The mean intensity for each annulus was assigned an uncertainty of

$$\sigma_{\text{mean}} = \frac{\sigma_{\text{pix}}}{\sqrt{N_{\text{pix}}/n_{\text{beam}}}} \quad (5)$$

where  $\sigma_{\text{pix}}$  and  $N_{\text{pix}}$  are the RMS pixel value and the number of pixels in the annulus, and  $n_{\text{beam}}$  is the number of pixels in each resolution element (“beam”). The resolution of the H $\alpha$  images was assumed to be 2'' (Gaussian FWHM). Note that  $\sigma_{\text{mean}}$  is a quantity which reflects only the dispersion in the values within each annulus, and thus reflects a combination of measurement errors and any intrinsic non-axisymmetry.

TABLE 5. ADOPTED ORIENTATION PARAMETERS

Galaxy	P.A. <sup>(a)</sup> (deg)	$i$ (deg)
NGC 4321	153	34
NGC 4414	159	55
NGC 4501	140	63
NGC 4736	295	35
NGC 5033	353	68
NGC 5055	98	63
NGC 5457	42	21

<sup>a</sup>Position angle of receding side of line of nodes, measured E from N.

##### 3.2.1. CO and H I Profiles

Since the CO and H I intensity images are generated from datacubes by a masking process, sampling effects make their noise properties somewhat unusual. Especially at large radii where few pixels survive the masking, the RMS fluctuation within an annulus (given by  $\sigma_{\text{mean}}$  above) can greatly underestimate the error in the profile because masked pixels have been assigned a value of zero. We can derive a conservative estimate of the true uncertainty in the mean for each annulus by considering the case in which all channels are included in the moment map (i.e., no masking or clipping of any kind):

$$\sigma_{\text{est}} = \frac{\sigma_{\text{ch}} \Delta v \sqrt{n_{\text{ch}}}}{\sqrt{N_{\text{pix}}/n_{\text{beam}}}} , \quad (6)$$

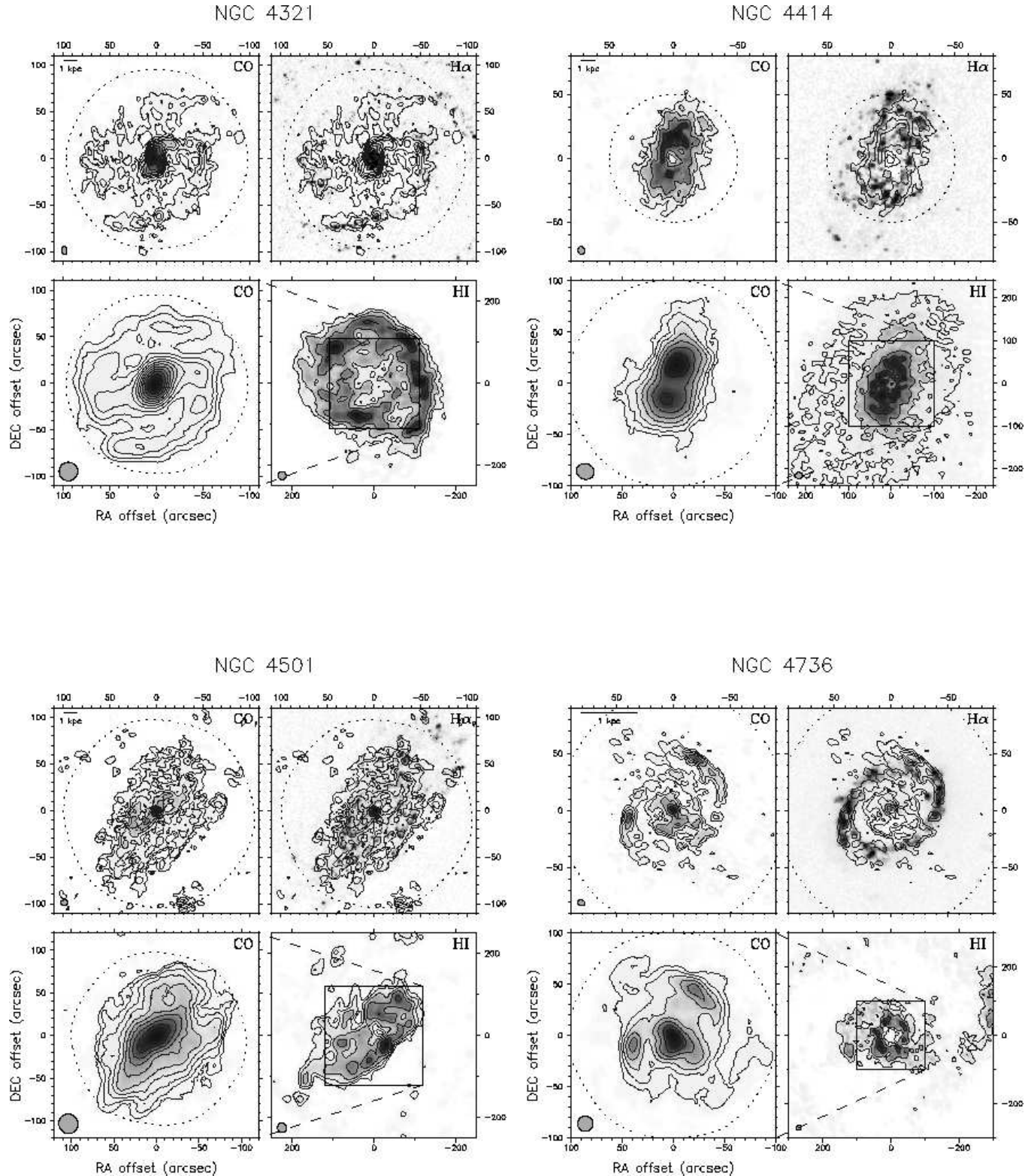
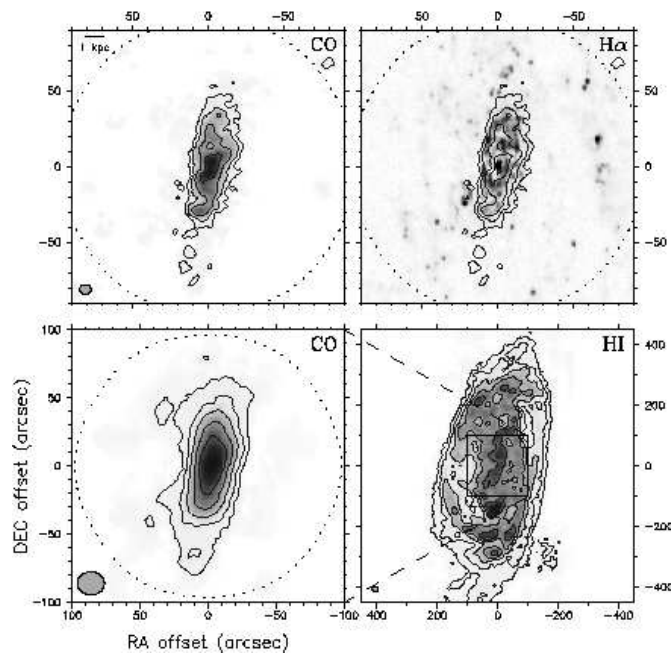
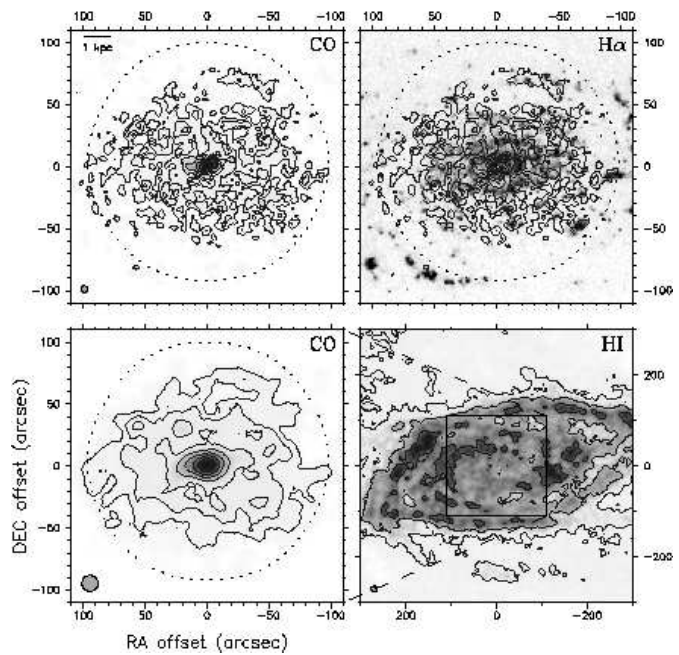


FIG. 2.— Intensity images for each of the seven galaxies in our sample. *Top left:* CO at full spatial resolution (robust or natural weighting). Contours are  $k_1 n^2$  Jy  $\text{km s}^{-1}$ , for integers  $n \geq 2$  and  $k_1=0.75$  for NGC 4321, 4414, and 4501,  $k_1=1$  for NGC 4736 and 5055,  $k_1=1.5$  for NGC 5033, and  $k_1=0.6$  for NGC 5457. *Top right:* H $\alpha$  image with CO contours overlaid. *Bottom left:* CO at the resolution of the H I image. Contour levels are  $k_2 n^2$  Jy  $\text{km s}^{-1}$ , for integers  $n \geq 2$  and  $k_2=2$  for NGC 4321, 4414, 4501, and 4736,  $k_2=4$  for NGC 5033,  $k_2=3$  for NGC 5055, and  $k_2=1$  for NGC 5457. *Bottom right:* H I intensity image, with contours of  $0.02n^2$  Jy  $\text{km s}^{-1}$  ( $n \geq 2$ ).

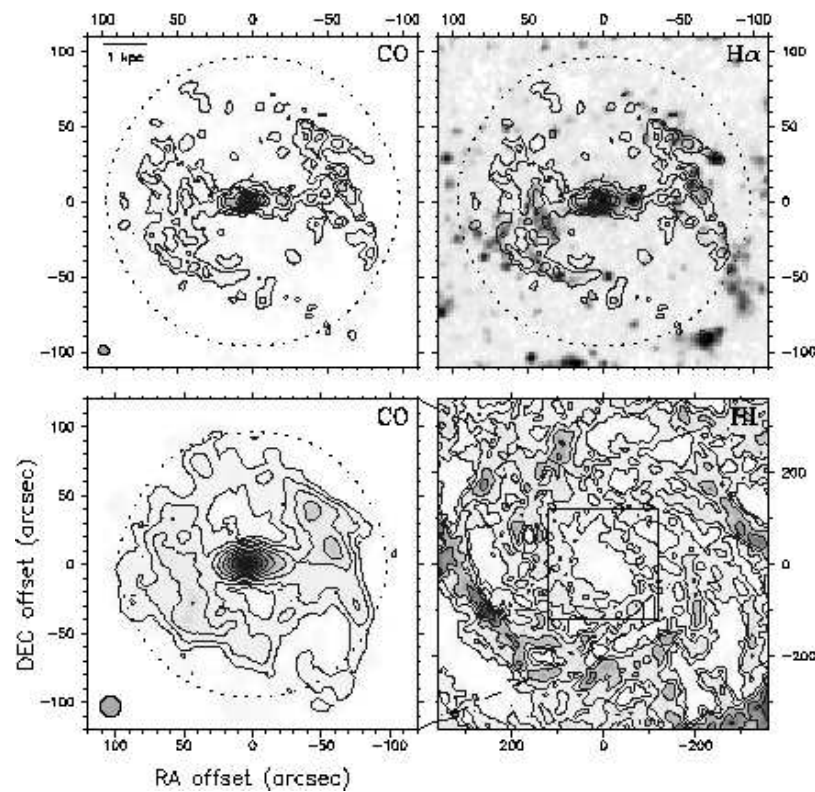
NGC 5033



NGC 5055



NGC 5457



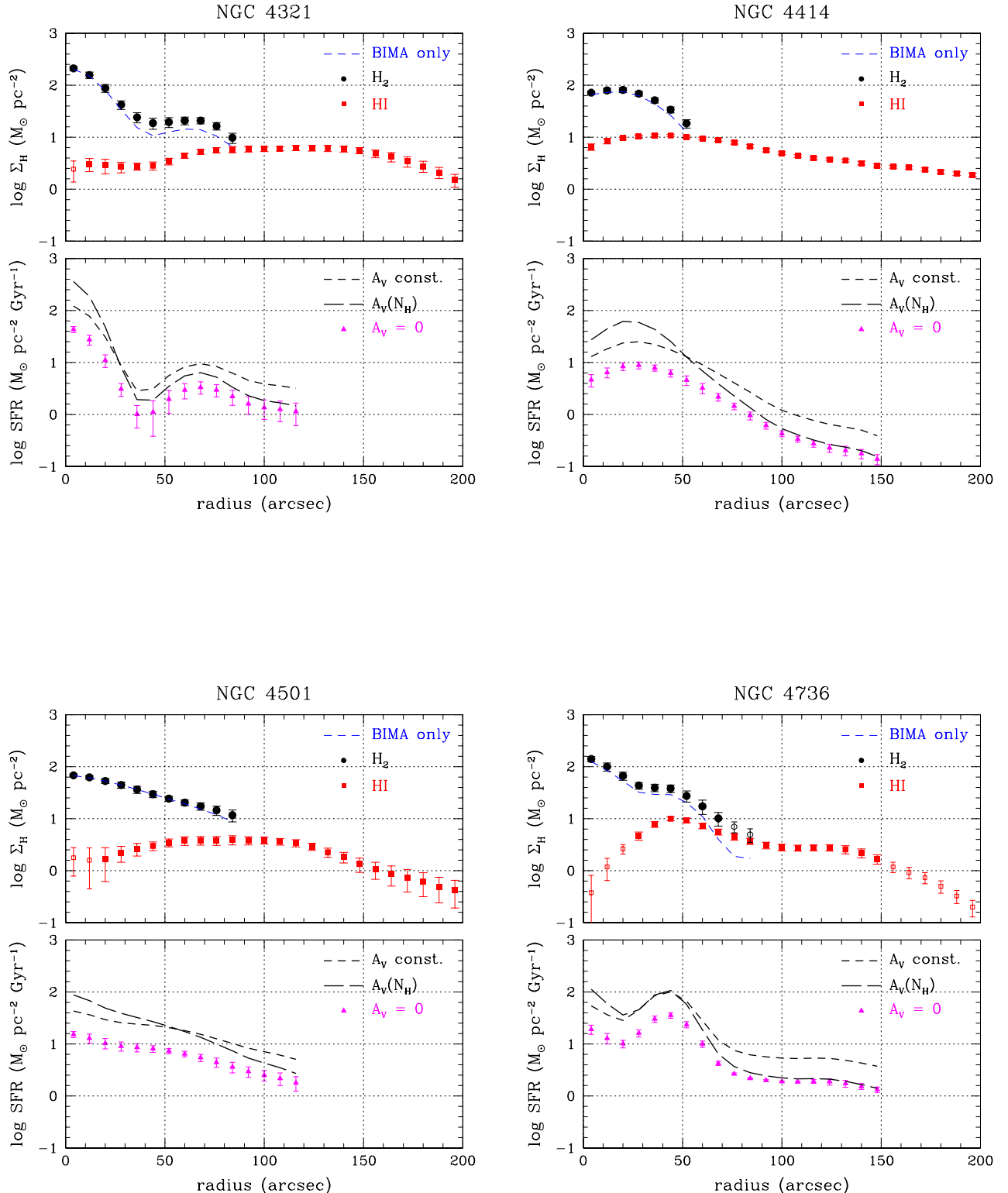
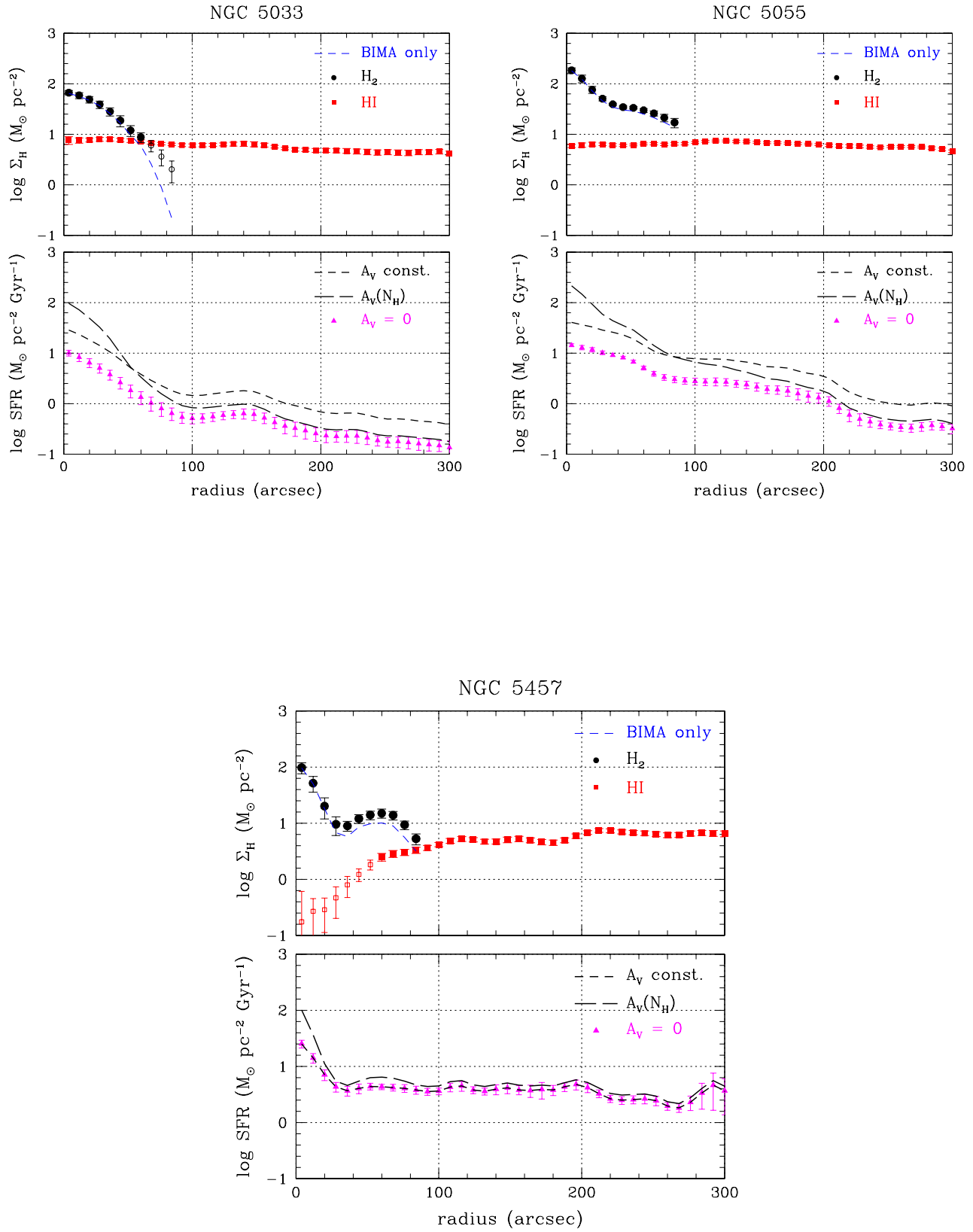


FIG. 3.— Radial profiles of H I, H<sub>2</sub>, and SFR surface density. *Top panels*: H I and H<sub>2</sub> profiles, corrected for inclination. The H<sub>2</sub> profile derived from the BIMA CO data alone is shown as a dashed line. Unfilled plot symbols represent uncertain measurements that may suffer from incompleteness (see text). *Bottom panels*: SFR profile (triangles), corrected for inclination but not for H $\alpha$  extinction. The short and long dashed lines are the resulting SFR for uniform and  $N_{\text{H}}$ -dependent extinction corrections respectively.



where  $\sigma_{\text{ch}}$  is the RMS noise in a channel map of the original datacube,  $n_{\text{ch}}$  is the number of channels, and  $\Delta v$  is the velocity width of each channel.

The derived radial gas profiles, at the resolution of the H I maps, are presented in the top panels of Figure 3. Points are separated by  $8''$ , oversampling the profiles slightly. Unfilled plot symbols are used to denote radii where the mean intensity falls below  $3\sigma_{\text{est}}$ , since these measurements are less secure, relying on the ability of the mask to select out the “real” emission. These radii are also the most likely to suffer from incompleteness, which can result if the mask excludes low-level emission that still makes a substantial contribution to the sum when integrated over a large annulus. The profiles are given in mass surface density units, which are derived as follows. First the conversion from surface brightness to column density is performed using the CO-to-H<sub>2</sub> conversion factor given by Equation 3, or using the optically thin approximation for H I:

$$N_{\text{HI}} = 1.82 \times 10^{18} \left( \frac{I_{21}}{\text{K km s}^{-1}} \right) \text{ cm}^{-2}, \quad (7)$$

where  $I_{21}$  is the velocity-integrated H I intensity. Column densities were then converted to face-on surface densities,

$$\Sigma_{\text{HI}} = m_{\text{H}} N_{\text{HI}} \cos i, \quad (8)$$

$$\Sigma_{\text{H}_2} = 2m_{\text{H}} N_{\text{H}_2} \cos i, \quad (9)$$

excluding helium. The BIMA-only CO profiles, converted to the appropriate units, are also shown for comparison. Note that the extra flux provided by the KP data has little effect on the CO radial profiles, aside from a constant offset which only becomes significant at outer radii.

The assumption of a constant CO-to-H<sub>2</sub> conversion factor ( $X$ -factor) remains quite controversial, with some researchers suggesting that  $X$  is increased by a factor of 10 or more in the vicinity of the Galactic Center (Sodroski et al. 1995; Dahmen et al. 1998). Indeed, the presence of central CO condensations in many galaxies (Sakamoto et al. 1999; Regan et al. 2001) may be an indication of a change in the  $X$ -factor rather than a true concentration of molecular gas. On the other hand, two of the seven galaxies (NGC 4501 and 5033) show featureless, roughly exponential CO profiles. We discuss the possibility of a varying  $X$ -factor further in §5.1.

### 3.2.2. Total Gas Profiles

Radial profiles of the total gas surface density ( $\Sigma_{\text{gas}}$ ) were derived by summing the contributions from H I and H<sub>2</sub> and multiplying a factor of 1.36 to include helium. Since the CO emission is only imaged within  $R \lesssim 2'$ , and our sensitivity to CO emission falls off at H<sub>2</sub> column densities comparable to the peak H I column densities of  $\sim 10 \text{ M}_{\odot} \text{ pc}^{-2}$ , it was necessary to extrapolate the CO profile to larger radii assuming an exponential profile. The scale length for the extrapolation was determined from a fit to the entire radial profile, except for NGC 4414, where the fit was made to the declining part of the CO profile, and NGC 5457, where the scale length was determined from the radial profile of a large ( $10' \times 10'$ ) CO map obtained at the NRAO 12m telescope as part of BIMA SONG. To take an example, Figure 4 shows the total gas profile for NGC 4321 and its individual components (also corrected for helium). The profiles are probably most uncertain at

radii just beyond  $R_{\text{max}}$  (refer to Table 2), where the extrapolated H<sub>2</sub> mass is likely to be significant. Even so, we expect molecular gas to contribute less than half of the gas mass at these radii, and hence the error in  $\Sigma_{\text{gas}}$  introduced by the extrapolation should be  $\lesssim 50\%$  as long as the CO profile continues to decline beyond  $R_{\text{max}}$ , an assumption supported by visual inspection of our somewhat larger OTF maps.

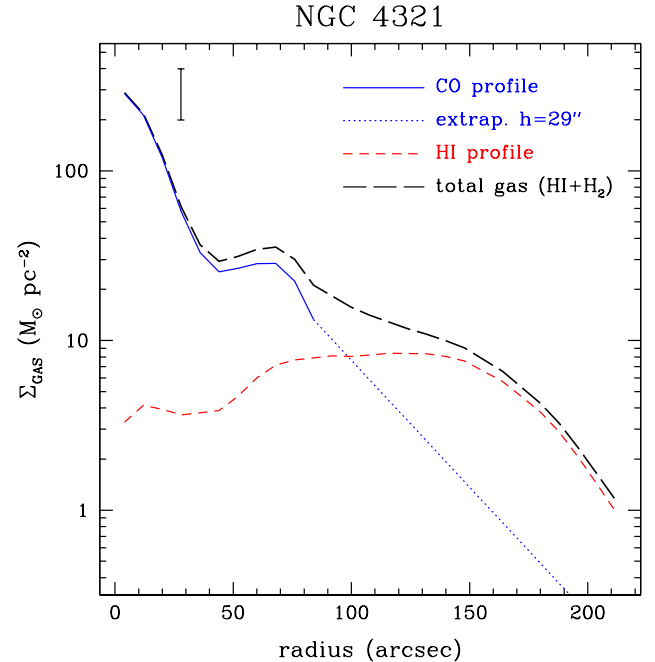


FIG. 4.— Total gas profile for NGC 4321 derived from the CO and H I profiles, with the CO profile extrapolated as shown. The error bar in the upper left corner represents a factor of 2 change in any of the curves.

### 3.2.3. H $\alpha$ Profiles

The H $\alpha$  emission from spiral galaxies is dominated by young ( $t < 20$  Myr), massive ( $> 10 \text{ M}_{\odot}$ ) stars, and is thus a reasonable tracer of the recent star formation rate (SFR) (see the review by Kennicutt 1998b). We expressed the H $\alpha$  brightnesses in units of SFR density using the conversion (Kennicutt 1998b):

$$\frac{\text{SFR}}{\text{M}_{\odot} \text{ yr}^{-1}} = 7.9 \times 10^{-42} \left( \frac{L_{\text{H}\alpha}}{\text{erg s}^{-1}} \right). \quad (10)$$

This conversion ignores extinction by dust and assumes a Salpeter IMF between  $0.1\text{--}100 \text{ M}_{\odot}$ , a constant SFR with time, and negligible escape of ionizing radiation from the galaxy. Since the H $\alpha$  images include a contribution from [N II], they have been multiplied by 0.67, assuming an average ratio of [N II]/H $\alpha \sim 0.5$  (Kennicutt 1992). Although the use of a uniform correction is rather simplistic, since [N II]/H $\alpha$  is often enhanced in the nuclear region (e.g., Rubin & Ford 1986), it should be roughly applicable for most of the H II regions in the disk. For comparison, Smith et al. (1991) used long-slit spectroscopy to deduce a ratio of H $\alpha$ /([N II]+H $\alpha$ )  $\approx 0.62$  for the star-forming ring in NGC 4736.

The bottom panels of Figure 3 show the radial H $\alpha$  profiles, converted to units of SFR density, derived from images smoothed to the same resolution as the H I images.

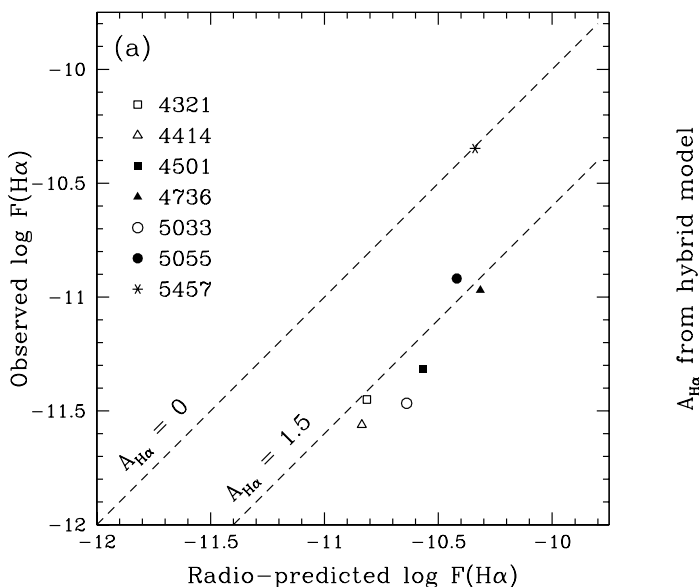
These can be directly compared to the gas profiles in the top panels. The data points have not been corrected for extinction, whereas the dashed lines represent the results of applying the extinction corrections described in §3.3. In §4.1.1 we also compare the CO and H $\alpha$  profiles at the higher resolution of the CO data, although we have not shown the corresponding profiles here.

### 3.3. Extinction Corrections for H $\alpha$

While extinction at H $\alpha$  due to Galactic dust along the line of sight is probably unimportant ( $A_{V, Gal} < 0.13$  mag for all seven galaxies according to Schlegel et al. 1998), extinction internal to the galaxies themselves is likely to be significant, given that stars form in regions of dense gas that have associated dust. Thus, when deriving quantitative estimates of the SFR from H $\alpha$  emission, it is important to take extinction into account.

In his study of disk-averaged star formation, K98 applied a constant extinction correction of 1.1 mag to his H $\alpha$  data, based on an earlier comparison of integrated H $\alpha$  and radio continuum fluxes (Kennicutt 1983). Although obviously a gross simplification, it is difficult to do better. The use of an H $\alpha$ /H $\beta$  ratio to determine the extinction is inapplicable for galaxy-integrated spectra, due to the difficulty of measuring the H $\beta$  flux in the presence of stellar absorption lines (Kennicutt 1992). Even with spectrophotometry of individual H II regions, one can typically only obtain measurements for the brightest sources, and the derived extinctions may not be appropriate for all of the H $\alpha$  emission (Bell & Kennicutt 2001). Hence, the most reliable extinction estimates are likely to come from narrow-band imaging of NIR recombination lines such as Br $\gamma$  or Pa $\alpha$ , or from measurements of thermal radio continuum fluxes.

We have considered four techniques for determining extinction corrections for our sample:



1. One can apply a global correction following K98, but instead using measured radio continuum and H $\alpha$  fluxes for individual galaxies. Niklas et al. (1995) published radio fluxes at 10 GHz for a large set of galaxies that encompasses our sample, and Niklas et al. (1997) have combined these with data at other frequencies to separate the thermal and non-thermal components (the latter often being dominant even at 10 GHz) via the spectral slope. The thermal flux  $S_{\text{th}}$  can be converted into a predicted H $\alpha$  flux using the formula (Condon 1992):

$$F_{\text{pred}}(\text{H}\alpha) = 8.0 \times 10^{-13} \left( \frac{\nu}{\text{GHz}} \right)^{0.1} \left( \frac{S_{\text{th}}}{\text{mJy}} \right) \text{ erg cm}^{-2} \text{ s}^{-1}. \quad (11)$$

This relation assumes an electron temperature of  $10^4$  K, but is not very sensitive to it ( $F_{\text{pred}} \propto T_e^{-0.5}$ ). In Figure 5(a) we compare the integrated fluxes in our H $\alpha$  images with the radio-predicted fluxes. While extinction appears to be negligible for NGC 5457 (M101), a typical value of  $A_{\text{H}\alpha} \sim 1.5$  mag is found for the other six galaxies. For these galaxies, the SFR is therefore underestimated by a factor of  $\sim 4$  when using the H $\alpha$  fluxes alone.

2. One can derive a radially dependent correction using the observed radial gas profile and an assumed dust-to-gas ratio. We first assume a “foreground dust screen model,” in which half of the observed gas column density is located in a uniform absorbing slab between the H $\alpha$  emission and us. We adopt standard Galactic values for the gas-to-dust ratio,  $N_{\text{H}}/A_V = 2 \times 10^{21} \text{ cm}^{-2} \text{ mag}^{-1}$ , and the extinction law,  $A_R/A_V = 0.75$  (Bohlin et al. 1978; Rieke & Lebofsky 1985). The inferred extinctions reach peak values of 4–14 mag near the galaxy center, although even these represent azimuthally averaged

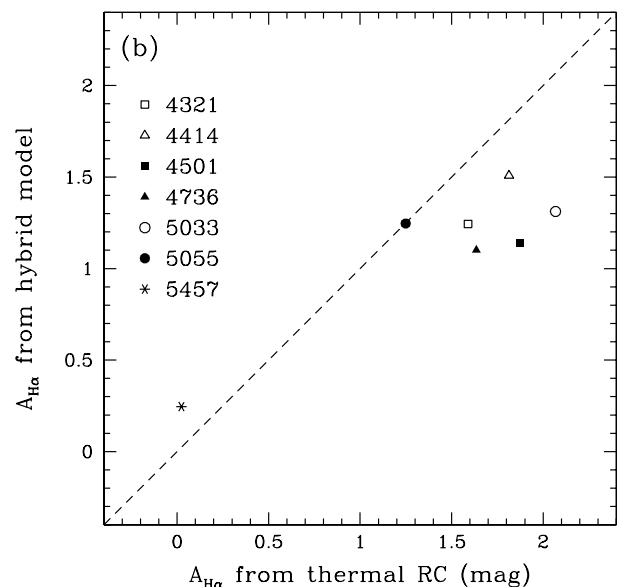


FIG. 5.— (a) Total H $\alpha$  flux for each galaxy (assuming [N II]/H $\alpha$ =0.5) plotted against the predicted H $\alpha$  flux based on the thermal radio continuum data. Dashed lines correspond to extinctions of 0 and 1.5 magnitudes. (b) Comparison of the disk-averaged extinction at H $\alpha$  derived from comparing the radio and H $\alpha$  fluxes with the extinction predicted by a “hybrid” dust model, where dust associated with H $_2$  is well-mixed but dust associated with H I constitutes a foreground screen. The model assumes a Galactic dust-to-gas ratio and extinction law. The dashed line has a slope of 1.

values at  $\sim 15''$  resolution. After correction for extinction, the global SFRs increase by factors ranging from 1.3 (for NGC 5457) to 140 (for NGC 5055). Comparing the disk-averaged extinction from this model to the radio-derived extinction, we find that for several galaxies, especially NGC 4321 and 5055, this method severely overestimates the global extinction, by up to 4 mag.

3. A simple alternative to the foreground dust screen model is a model in which the stars, gas, and dust are uniformly mixed. This model is motivated by the expectation that  $\text{H}\alpha$  traces stars which have recently formed from molecular gas, so the  $\text{H}\alpha$  and dust are likely to be physically co-extensive. For this case we have (e.g., Lequeux et al. 1981):

$$A_V = 2.5 \log \frac{\tau}{1 - e^{-\tau}} \quad (12)$$

where  $\tau$  is the extinction optical depth, again derived from the standard Galactic extinction law,  $\tau = A_V/1.086 = N_{\text{H}}[\text{cm}^{-2}]/(2.17 \times 10^{21})$ . In the limit of small optical depth, this reproduces the foreground screen model,  $A_V = 2.5 \log e^{\tau/2}$ , whereas for large  $\tau$ ,  $A_V$  increases  $\propto \log \tau$  rather than  $\propto \tau$ . This leads to much smaller extinction corrections at high gas densities, and closer agreement with the radio-derived extinctions. However, it appears to systematically underestimate the extinction for the galaxies with large  $A_V$  (e.g., NGC 5033).

4. Finally, we consider a “hybrid” model in which the  $\text{H}_2$  is mixed with the stars (Eq. 12) but the  $\text{H}$  I acts as a foreground screen, motivated by the larger scale height of the  $\text{H}$  I layer. When globally averaged, this leads to reasonable agreement (within  $\sim 0.5$  mag) with the radio-inferred extinctions, as shown in Figure 5(b).

For the analyses in this paper we will employ both methods (1) and (4). Method (1), a uniform correction across the galaxy, has the advantage that it is based directly on measurements (of  $\text{H}\alpha$  and radio fluxes) and agrees with previous studies that have found at most a weak trend in  $\text{H}$  II region extinction with galactocentric radius in M51 and NGC 6946 (e.g., van der Hulst et al. 1988; Belley & Roy 1992; Hyman et al. 2000). Method (4), which presupposes a correlation between gas column density and extinction, agrees roughly with the radio fluxes but is not based on actual extinction measurements. If incorrect, it may lead to a spurious relationship between the gas density and star formation rate—hence the importance of applying both methods. The results of applying methods (1) and (4) to the radial SFR profiles are shown by the short-dashed and long-dashed lines respectively in the lower panels of Fig. 3.

A recent study by Quillen & Yukita (2001), based on a comparison of  $\text{H}\alpha$  with *HST*  $\text{Pa}\alpha$  imaging of a number of galaxies, including the CO-rich spirals NGC 2903, M51, and NGC 6946, lends some support to method (4). They find that the foreground screen model accurately predicts  $A_{\text{H}\alpha}$  at low gas surface densities but overpredicts it at high densities. This is exactly the type of behavior provided by our hybrid model, since the low- $\Sigma_{\text{H}}$  regions are dominated

by  $\text{H}$  I whereas high- $\Sigma_{\text{H}}$  regions are dominated by  $\text{H}_2$ . Moreover, the typical extinctions in the central regions of their galaxies are  $A_V \sim 2\text{--}4$ , consistent with the radial extinction profiles derived using method (4). It is worth noting that NIR recombination-line studies seldom reveal bright  $\text{H}$  II regions suffering extinctions of  $A_V > 4$ , even in circumnuclear starbursts (e.g., Kotilainen et al. 2000) or in situations where much larger extinctions might be expected based on the gas surface density (Krabbe et al. 1994).

Our extinction corrections may still underestimate the SFR if a substantial fraction of Lyman continuum photons escape from galaxies or are absorbed by dust within the  $\text{H}$  II regions themselves, since such photons will not lead to observable  $\text{H}\alpha$  or radio continuum emission. The first effect, escape from the galaxy as a whole, is likely to be small—for example, Dove & Shull (1994) estimate an escape fraction for the Milky Way of  $\sim 14\%$  (but see Beckman et al. 2000 for a contrasting view). While this fraction may vary with radius, Ferguson et al. (1996) find little variation in the diffuse  $\text{H}\alpha$  fraction with radius, a quantity which they argue measures leakage of Lyman continuum photons. As for the second effect, dust absorption, Mathis (1986) estimates a typical optical depth to Lyman continuum photons in  $\text{H}$  II regions of  $\tau \sim 1.4$ , in which case we have underestimated the SFR by up to a factor of  $\sim 4$ . An analysis by McKee & Williams (1997), however, indicates that such absorption is less significant in  $\text{H}$  II region envelopes than within the Strömgren radius; globally they find only  $\sim 25\%$  of ionizing photons are absorbed by dust, yielding a correction factor of 1.37. Given the present lack of consensus, we apply no further corrections but note that our SFR estimates may be somewhat low.

## 4. RESULTS

### 4.1. The Star Formation Law

Using the radial profiles of CO,  $\text{H}$  I, and total gas density derived in §3.2, we can compare the gas surface density with the observed SFR surface density (derived from the  $\text{H}\alpha$  profile) on a ring-by-ring basis. Such a comparison involves averaging over greater areas for outer rings as opposed to inner rings, and thus both random and systematic errors will vary with radius. In particular, the lack of independent data points may be a problem in the inner rings, whereas errors in flat-fielding or masking may dominate for outer rings. To minimize the impact of our masking method, we have only taken the radial profiles where they exceed the  $3\sigma_{\text{est}}$  level defined in Equation 6. We note that despite their limitations, radial profiles are fairly insensitive to angular resolution and permit one to effectively average over time, which can be useful for revealing overall trends. A point-by-point comparison of gas and star formation would be quite sensitive to the map resolution and to evolutionary effects, since on small enough scales,  $\text{H}$  II regions will disrupt their natal clouds. In a future paper, we will consider additional techniques for analyzing the two-dimensional intensity maps for both  $\Sigma_{\text{gas}}$  and  $\Sigma_{\text{SFR}}$  provided by BIMA SONG.

#### 4.1.1. The SFR and Molecular vs. Atomic Gas

We first consider the relationships between  $\Sigma_{\text{SFR}}$  and the atomic and molecular surface densities,  $\Sigma_{\text{HI}}$  and  $\Sigma_{\text{H}_2}$ ,

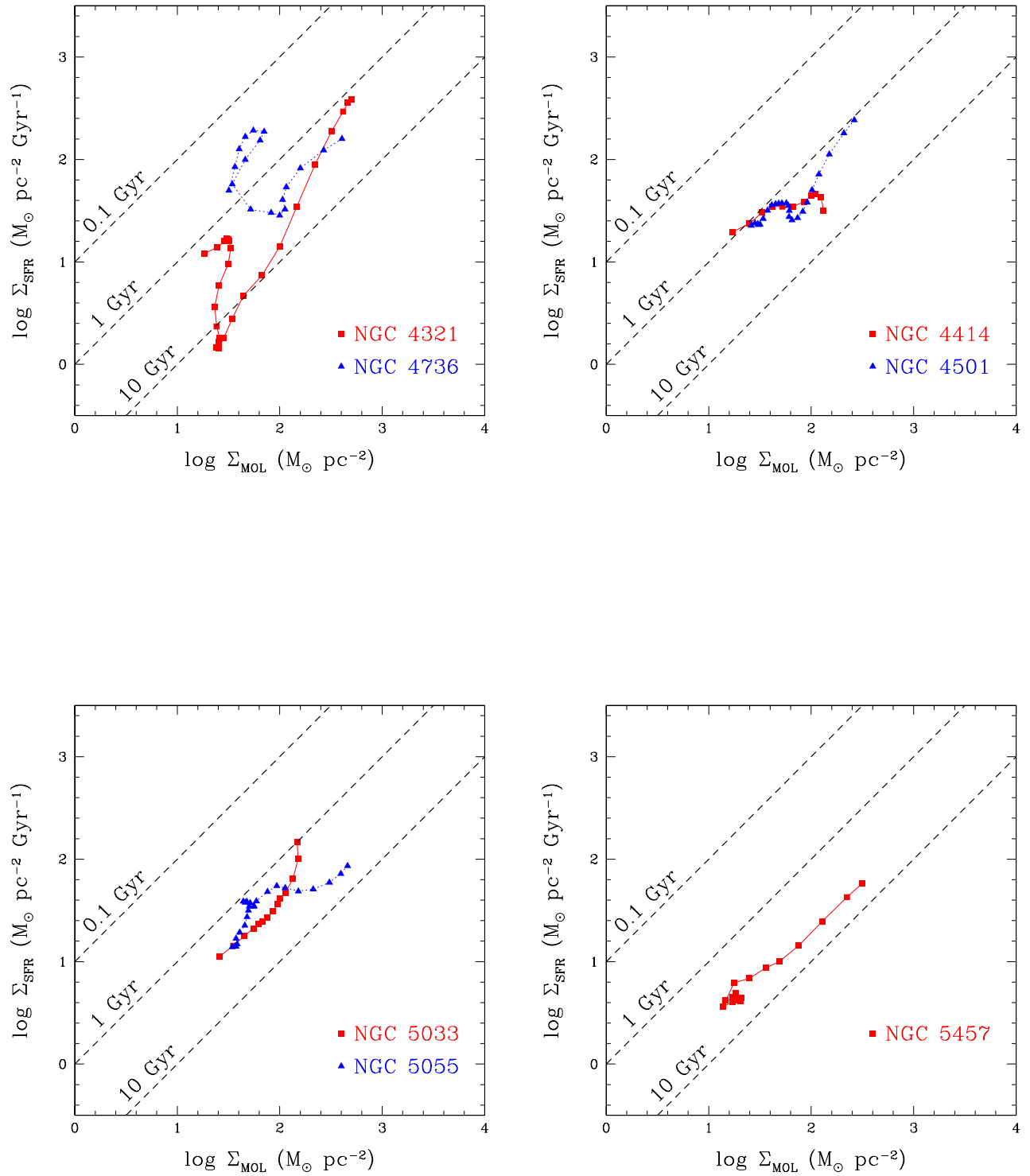


FIG. 6.— SFR plotted against  $\text{H}_2$  gas density (including associated helium), with both quantities azimuthally averaged, for the uniform extinction model. Dashed lines represent lines of constant star formation efficiency, with the corresponding gas depletion time labeled (assuming  $\text{H}_2$  is the only fuel for star formation). Note that we have taken advantage of the higher resolution ( $\sim 6''$ ) of the CO data in making the comparison.

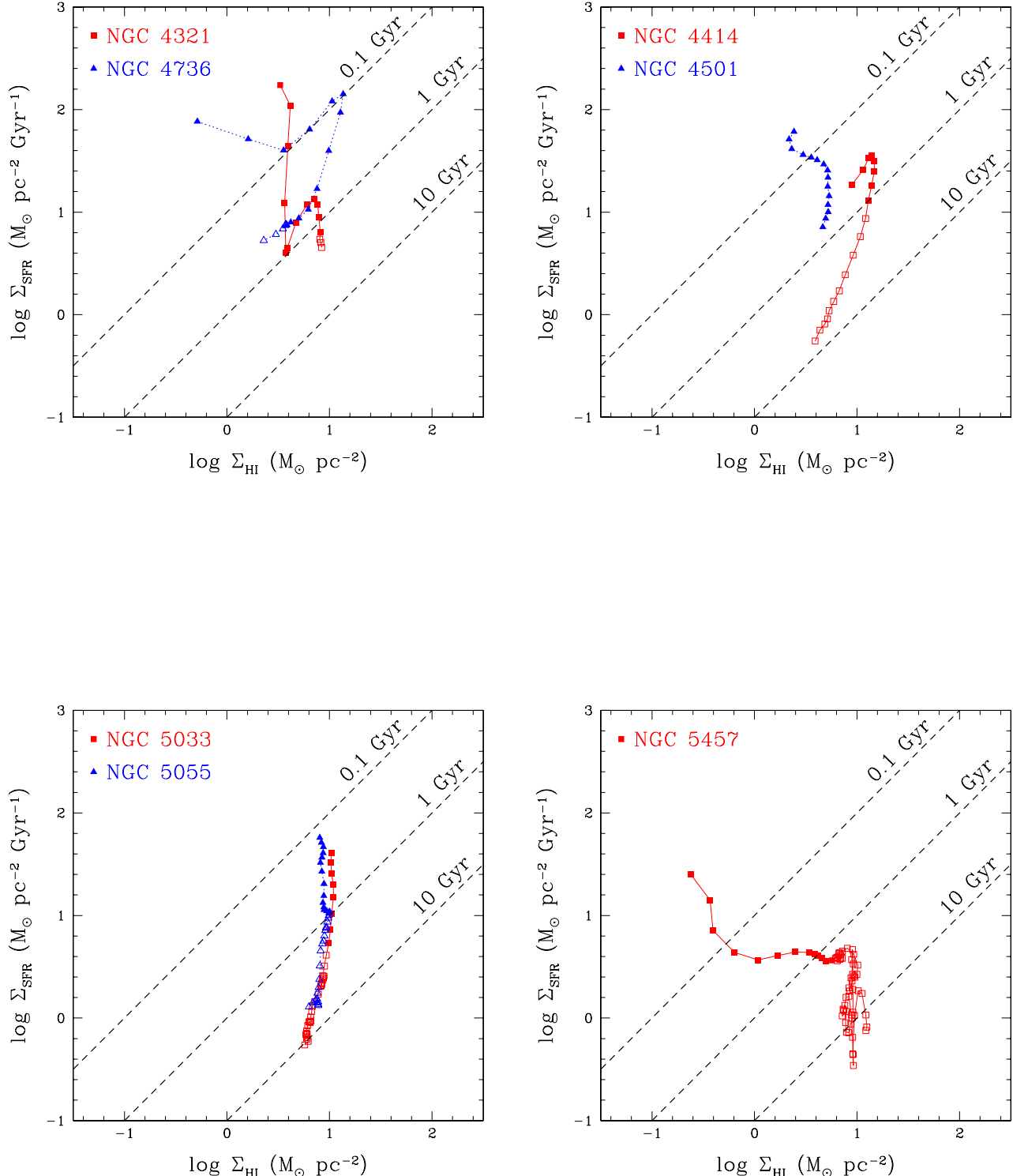


FIG. 7.— SFR plotted against H I gas density (including associated helium), with both quantities azimuthally averaged, for the uniform extinction model. Open symbols represent points where the molecular fraction is  $<0.5$ . Dashed lines represent lines of constant star formation efficiency, with the corresponding gas depletion time labeled (assuming H I is the only fuel for star formation).

separately. One advantage of such comparisons is that they avoid ambiguities resulting from the extrapolation of the CO profile; moreover, the comparison with  $\Sigma_{\text{H}_2}$  can be made at the higher resolution of the BIMA data. As described in §3.3, we consider two ways of correcting the  $\text{H}\alpha$  data for extinction: applying a uniform correction across the disk, or a radially varying correction that depends on the average gas column density. While the latter method may seem more physically motivated, evidence for radial extinction gradients is inconclusive at present. The results for the uniform extinction model are shown in Figures 6 and 7, with up to two galaxies shown per panel.

Most galaxies exhibit an excellent correlation between azimuthally averaged  $\text{H}\alpha$  and CO emission that can be parametrized using a Schmidt (power) law:

$$n_{\text{mol}} = \frac{d \log \Sigma_{\text{SFR}}}{d \log \Sigma_{\text{mol}}} , \quad (13)$$

For the  $N_{\text{H}}$ -dependent extinction corrections, the inferred power-law indices range from  $n_{\text{mol}} \approx 1$  for NGC 4414 to  $n_{\text{mol}} \approx 2$  for NGC 5033 (see Table 5). The two exceptions are NGC 4321, where the SFR is suppressed in the vicinity of a bar ( $R=15''-55''$ , where  $\log \Sigma_{\text{mol}} \approx 1.4$ ), and NGC 4736, where the SFR is enhanced near a resonance ring ( $R=30''-55''$ , where  $\log \Sigma_{\text{mol}} \approx 1.6$ ). These examples suggest that the molecular content alone does not always control the SFR—dynamical effects can also be important (see e.g., Wong & Blitz 2000; Meier & Turner 2001). Even in NGC 4321 and 4736, however, there are regions where a power-law relationship is roughly obeyed. A weighted average for all seven galaxies gives  $\bar{n}_{\text{mol}}=0.8$  for the uniform extinction model and  $\bar{n}_{\text{mol}}=1.4$  for the varying extinction model. For comparison, Rownd & Young (1999) made point-by-point CO and  $\text{H}\alpha$  comparisons for over 100 galaxies at  $45''$  resolution, and found  $n_{\text{mol}}=1.2-1.4$  with no extinction corrections applied. However, they note that  $n_{\text{mol}}=1$  (constant SFE for the molecular gas) is not excluded by their data. Assuming  $A_V$  does not vary strongly with radius, our study also finds reasonable agreement with a law in which the SFR per unit area is proportional to the molecular gas surface density.

The relationship between  $\Sigma_{\text{SFR}}$  and  $\Sigma_{\text{HI}}$  is more complex and appears inconsistent with a Schmidt law. In some cases, there is an abrupt decline in  $\Sigma_{\text{HI}}$  even when  $\Sigma_{\text{SFR}}$  is fairly high (NGC 4736 and 5457, and to a lesser extent NGC 4414 and 4501). These galaxies have central  $\text{H}\text{I}$  depressions where significant star formation is still occurring. In other cases, the value of  $\Sigma_{\text{HI}}$  stays fairly constant over a wide range in  $\Sigma_{\text{SFR}}$ , suggesting that a maximum value of  $\Sigma_{\text{HI}}$  has been reached. This maximum value, roughly  $10 \text{ M}_\odot \text{ pc}^{-2}$  or  $N_{\text{HI}} \sim 10^{21} \text{ atoms cm}^{-2}$ , could result from a tendency for  $\text{H}\text{I}$  to convert to  $\text{H}_2$  at higher column densities due to self-shielding (Federman et al. 1979; Shaya & Federman 1987). Alternatively, the optical depth in the 21-cm line could become substantial above this column density, especially if a cold  $\text{H}\text{I}$  component dominates (e.g., Braun 1997). The opacity at the line center is given by (Dickey & Lockman 1990):

$$\tau = 5.2 \times 10^{-19} \left( \frac{N_{\text{HI}}}{T \Delta v} \right) , \quad (14)$$

which produces  $\tau=1$  at  $N_{\text{HI}}=10^{21} \text{ cm}^{-2}$  for  $T=50 \text{ K}$  and  $\Delta v=10 \text{ km s}^{-1}$ . However, Fig. 3 suggests that the maximum deprojected  $N_{\text{HI}}$  is not dependent on inclination

as one would expect if it were an optical depth effect: NGC 5033 ( $\cos i=0.37$ ) and 5457 ( $\cos i=0.93$ ) both exhibit azimuthally averaged  $\text{H}\text{I}$  surface densities that plateau around  $\sim 6-8 \text{ M}_\odot \text{ pc}^{-2}$ .

Surprisingly, Kennicutt (1989, 1998a) has found that the disk-averaged SFR is more strongly correlated with the disk-averaged  $\text{H}\text{I}$  surface density than with the CO surface density. Similar conclusions were drawn by Deharveng et al. (1994), who traced the SFR using far-ultraviolet (FUV) data, and Boselli (1994), who used both FUV and  $\text{H}\alpha$ . Our study, based on fully-sampled CO maps, is not consistent with these findings. The lack of a correlation between  $\Sigma_{\text{SFR}}$  and  $\Sigma_{\text{HI}}$  in our data may result from a bias in our sample towards molecule-rich galaxies, where the  $\text{H}\text{I}$  surface density tends to saturate at a value of  $\sim 10 \text{ M}_\odot \text{ pc}^{-2}$ . Galaxies with substantially less molecular gas may show a wider range of  $\Sigma_{\text{HI}}$ . It is more difficult to understand why the correlation between global CO flux and SFR found by Kennicutt and others should be so poor, but K98 notes that the correlation is improved when only metal-rich spirals (such as those in our sample) are considered, an effect he attributes to variations in the CO-to- $\text{H}_2$  conversion factor ( $X$ -factor). Furthermore, the inhomogeneity of the CO distribution in most galaxies suggests that incorrect  $\text{H}_2$  masses may be derived when the CO distribution is not completely mapped.

#### 4.1.2. The SFR and the Total Gas Surface Density

Combining the CO and  $\text{H}\text{I}$  data (with the CO profile extrapolated to larger radii) enables us to compare the SFR surface density with the *total* gas surface density, which has been argued to be a more relevant quantity for star formation than  $\Sigma_{\text{H}_2}$  alone (Kennicutt 1989; K98). Figure 8 shows the radial profiles for all seven galaxies as plotted in the  $\Sigma_{\text{gas}}-\Sigma_{\text{SFR}}$  plane for the two extinction models. Regardless of how extinction is treated, there is indeed a strong correlation between  $\Sigma_{\text{gas}}$  and  $\Sigma_{\text{SFR}}$  within galaxies, indicative of a Schmidt law (Eq. 1). As is clear from the results of §4.1.1, however, this correlation is driven entirely by the molecular component for these galaxies, as  $\Sigma_{\text{SFR}}$  shows virtually no correlation with  $\Sigma_{\text{HI}}$ . We note that the situation may be different in galaxies where the ISM is predominantly atomic, and further studies should be aimed at exploring the connection between star formation and the  $\text{H}\text{I}$  component in such galaxies.

Also shown in Fig. 8 as a dashed line is the composite Schmidt law derived by K98,

$$\Sigma_{\text{SFR}} = 0.16 \left( \frac{\Sigma_{\text{gas}}}{1 \text{ M}_\odot \text{ pc}^{-2}} \right)^{1.4} \text{ M}_\odot \text{ Gyr}^{-1} \text{ pc}^{-2} . \quad (15)$$

(Note that the numerical coefficient has been adjusted to include helium in  $\Sigma_{\text{gas}}$ .) Kennicutt's parameterization is based on averages over the star-forming disks of 61 normal galaxies and the inner  $\sim 1 \text{ kpc}$  disks of 36 starbursts. Two features are evident from Fig. 8. First, the use of an  $N_{\text{H}}$ -dependent extinction correction produces a steeper dependence of  $\Sigma_{\text{gas}}$  on  $\Sigma_{\text{SFR}}$  than a uniform correction, as would be expected (e.g., Buat et al. 1989). Second, most of the observed data points lie to the right of Kennicutt's relation. Note, however, that many of the points at larger  $\Sigma_{\text{gas}}$  in Fig. 8 occur at inner radii, which are weighted

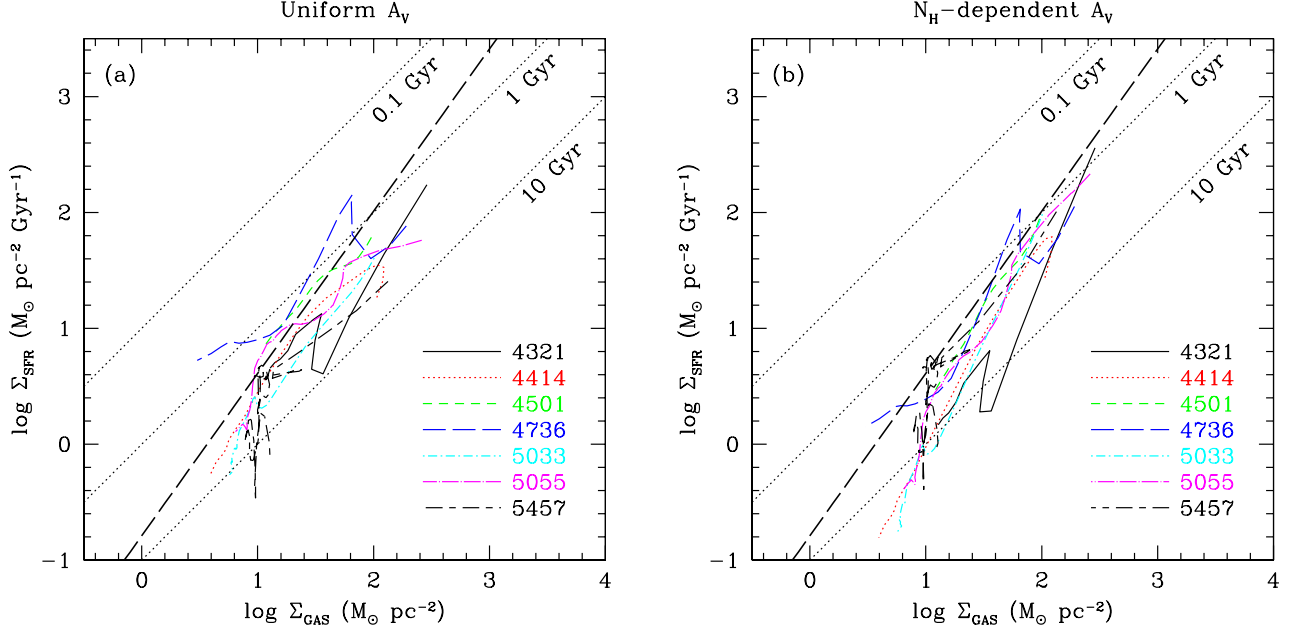


FIG. 8.— SFR plotted against total gas density for rings within all seven galaxies, after applying (a) uniform extinction corrections; (b)  $N_H$ -dependent extinction corrections. Parallel dotted lines represent lines of constant SFR per unit gas mass, with the corresponding gas depletion time labeled. The heavy dashed line is the global Schmidt law derived by K98.

less when taking a global average. Averaging our data across the entire observed disk region leads to much better agreement with Kennicutt's results (Figure 9), even though our outer radius is generally smaller than the optical radius adopted by K98. Indeed, we find that the offsets between our disk-averaged values and Kennicutt's points for the same galaxies in Fig. 9 can largely be attributed to a change in the normalizing radius, which shifts points along a line of unit slope for the same total SFR and  $M_{\text{gas}}$ . We conclude that within the uncertainty of  $\pm 0.2$  dex adopted by K98, our results are consistent with his.

Table 5 gives the average Schmidt law index,

$$n = \frac{d \log \Sigma_{\text{SFR}}}{d \log \Sigma_{\text{gas}}}, \quad (16)$$

within each galaxy as derived from an unweighted least-squares fit to the curves in Fig. 8. An average of the indices for all seven galaxies, weighted by the inverse of their variances, gives  $\bar{n} = 1.1 \pm 0.2$  for the uniform extinction model and  $\bar{n} = 1.7 \pm 0.3$  for the  $N_H$ -dependent extinction model. We examined the effect of changing the radial CO profile in the region where it had been extrapolated: in the extreme cases of a sharp truncation or complete flattening of the CO profile, we obtained values of  $\bar{n} = 0.8$  and 1.45 respectively for the uniform extinction model. However, such extreme profiles seem unlikely, and we consider the  $1\sigma$  errors on  $\bar{n}$  stated above to be realistic. Given the uncertainties, our derived indices are roughly consistent with the Schmidt law *among* galaxies ( $n \approx 1.4$ ) found by K98. Note that there would not necessarily have been a correspondence between the azimuthally averaged and global Schmidt laws if star formation in galaxies depended on some quantity other than  $\Sigma_{\text{gas}}$ , but for which a disk-averaged  $\langle \Sigma_{\text{gas}} \rangle$  was a convenient proxy. Thus, the validity of the Schmidt law on both local and global scales probably reflects an underlying physical link between  $\Sigma_{\text{gas}}$  and  $\Sigma_{\text{SFR}}$ .

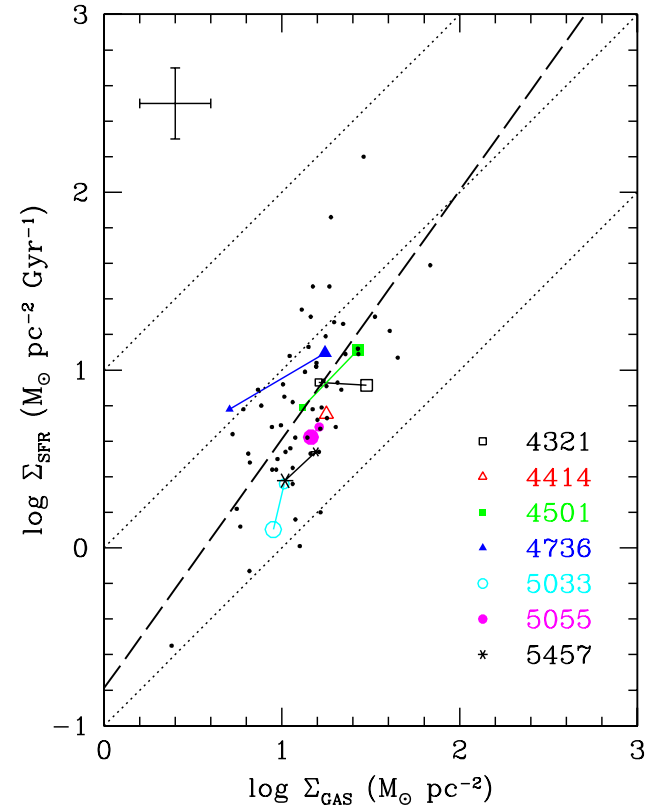


FIG. 9.— Disk-averaged SFRs plotted against total gas density. Large plot symbols are averages derived from radial profiles given in this paper, with radially varying extinction corrections applied. When connected by a line to a smaller symbol, the small symbol represents the corresponding point for the same galaxy as given by K98. The small dots are the other disk averages calculated by K98, the heavy dashed line is his global Schmidt law, and the error bars in the upper left represent his estimate of the uncertainties.

TABLE 5  
OBSERVED SCHMIDT LAW INDICES FOR TOTAL GAS AND H<sub>2</sub> ONLY

Galaxy	total gas		molecular gas	
	$A_V$ const.	$A_V(N_H)$	$A_V$ const.	$A_V(N_H)$
NGC 4321	1.13±.12	1.74±.14	1.41±.16	2.08±.16
NGC 4414	1.15±.07	1.71±.05	0.32±.06	0.98±.06
NGC 4501	0.95±.04	1.60±.03	0.90±.10	1.63±.10
NGC 4736	0.82±.09	1.23±.09	0.04±.24	0.74±.24
NGC 5033	1.38±.04	2.06±.04	1.27±.13	2.01±.13
NGC 5055	1.14±.07	1.79±.06	0.55±.08	1.30±.08
NGC 5457	1.18±.17	1.56±.17	0.88±.03	1.45±.04
Weighted Avg.	1.12±.22	1.75±.25	0.78±.34	1.36±.35

#### 4.1.3. Gas Depletion vs. Orbital Timescales

We have also considered an alternative description of the star formation law given by

$$\Sigma_{\text{SFR}} \propto \Sigma_{\text{gas}} \Omega, \quad (17)$$

where  $\Omega$  is the orbital frequency (e.g., Larson 1988; Silk 1997). This law can be expressed as

$$\tau_{\text{orb}} = \epsilon \tau_{\text{gas}}, \quad (18)$$

where  $\tau_{\text{gas}} \equiv \Sigma_{\text{gas}} / \Sigma_{\text{SFR}}$  is the timescale for gas depletion by star formation,  $\tau_{\text{orb}}$  is the orbital period and  $\epsilon$  is an efficiency factor that represents the fraction of available gas that is consumed in each orbit. K98 finds that Equation 18, with  $\epsilon \sim 0.1$ , provides an equally good fit to the disk-averaged data in comparison to the Schmidt law. However, this prescription can only be properly tested using azimuthally averaged data *within* galaxies, since a disk-averaged  $\langle \tau_{\text{orb}} \rangle$  may simply be a reflection of the galaxy's dynamical mass.

Figure 10 shows the relation between  $\tau_{\text{orb}}$  and  $\tau_{\text{gas}}$  for the two extinction models we are considering.  $\tau_{\text{orb}}$  was determined from rotation curves fitted to the CO and H I velocity fields, which had been derived from the datacubes by an automated Gaussian fitting routine (details will be given in Paper II). Only points where  $R > 30''$  have been plotted, since inside of that region the adopted rotation curve has a higher spatial resolution than the total gas profile. Applying a uniform extinction, we find that although a roughly linear trend *among* galaxies is apparent, as found by K98, no strong linear relation exists *within* galaxies. This is not surprising, since  $\tau_{\text{gas}}$  tends to be constant with radius when uniform extinction corrections were applied, whereas Eq. 18 predicts  $\tau_{\text{gas}} \propto R$  for a flat rotation curve. The correlation improves somewhat for the varying extinction model [Fig. 10(b)], and indeed the scatter in  $\log[\Sigma_{\text{SFR}} / (\Sigma_{\text{gas}} \Omega)]$  is comparable to the scatter in  $\log(\Sigma_{\text{SFR}} / \Sigma_{\text{gas}}^{1.4})$  for this model. Thus a star formation law where  $\tau_{\text{gas}} \propto \tau_{\text{orb}}$  appears to be as valid a prescription

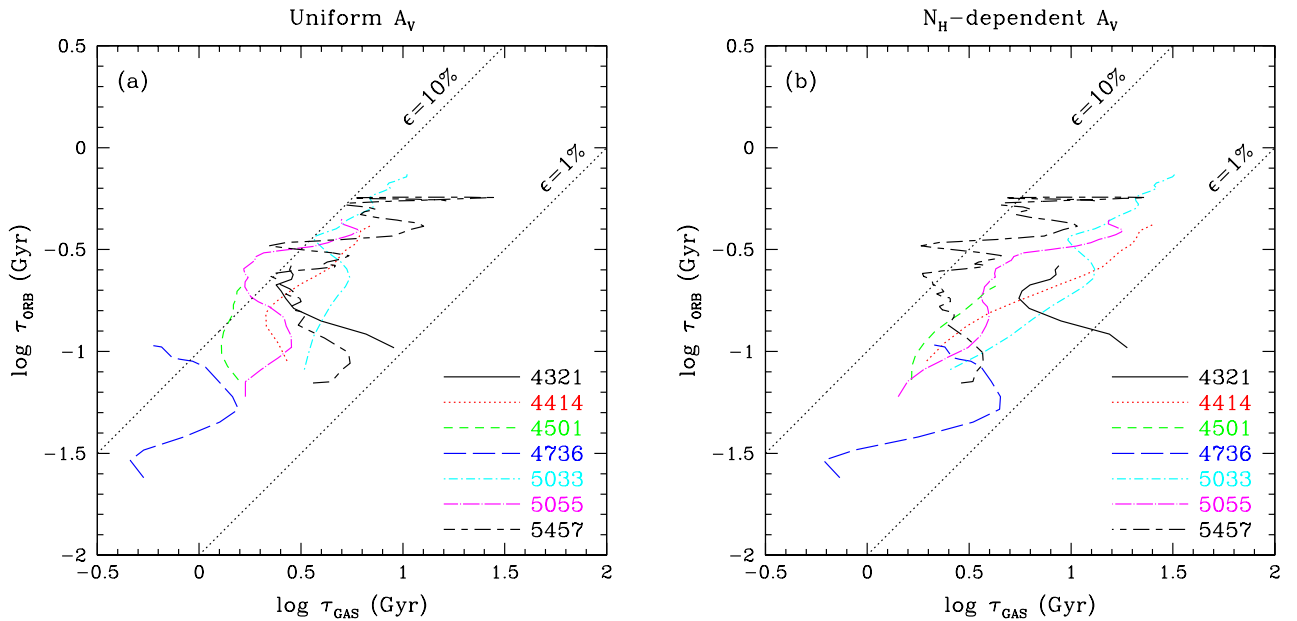


FIG. 10.—Orbital period  $\tau_{\text{orb}} = 2\pi/\Omega$  plotted against gas depletion time  $\tau_{\text{gas}}$  for annuli within each of the seven galaxies, after applying (a) uniform extinction corrections; (b)  $N_H$ -dependent extinction corrections. Parallel dotted lines denote points where 1% or 10% of the available gas is consumed by star formation during each orbit.

for the SFR as the Schmidt law, but only if the extinction increases towards the center to allow for a significant gradient in  $\tau_{\text{gas}}$ . To truly distinguish between the two prescriptions will require better constraints on the extinction, or the use of star formation tracers impervious to extinction.

#### 4.2. Star Formation Thresholds

Is star formation suppressed below a threshold or “critical” gas density? The observation that H I in spiral galaxies often extends well beyond the optical disk has led to widespread support for the notion of a star formation threshold that is constant or depends on local conditions. As proposed by Quirk (1972), such a threshold may be related to the parameter  $Q_g$  for gravitational instability in the gas layer (Safranov 1960; Toomre 1964):

$$Q_g \equiv \frac{\Sigma_{\text{crit}}}{\Sigma_{\text{gas}}}, \quad \text{where} \quad \Sigma_{\text{crit}} = \frac{\kappa c_g}{\pi G}. \quad (19)$$

Here  $\kappa$  is the epicyclic frequency and  $c_g$  is the gas velocity dispersion. For a thin gaseous disk, values of  $Q_g > 1$  correspond to stability and  $Q_g < 1$  to instability. Kennicutt (1989) found that in a sample of 15 mostly late-type galaxies, massive star formation was limited to regions of the disk where  $Q_g \lesssim 1.6$ , suggesting that gas beyond some threshold radius is no longer susceptible to gravitational instability. Within the star-forming part of the disk, he also found that  $Q_g$  did not vary much as function of radius, suggesting that star formation is self-regulated so that  $Q_g \sim 1$ .

We constructed radial profiles for  $\Sigma_{\text{crit}}$  using the adopted rotation curves presented in Paper II. The epicyclic frequency  $\kappa$  is given by

$$\kappa^2 = \frac{2v_c}{R} \left( \frac{dv_c}{dR} + \frac{v_c}{R} \right). \quad (20)$$

Note that for a flat rotation curve,  $\kappa^2 = 2\Omega^2$ . The derivative of the rotation curve was determined by simple two-point interpolation. Following Kennicutt (1989), we assumed a value of 6 km s<sup>-1</sup> for the velocity dispersion  $c_g$ , which is consistent with detailed observations of H I in the outer regions of NGC 1058 (van der Kruit & Shostak 1984; Dickey et al. 1990) and of CO in NGC 628 (Combes & Becquaert 1997). The resulting profiles of  $\Sigma_{\text{crit}}$  are shown in Figures 11–12, along with profiles for  $\Sigma_{\text{gas}}$  and  $\Sigma_{\text{SFR}}$ . Note that  $\Sigma_{\text{crit}} \propto R^{-1}$  for most galaxies, a reflection of the relatively flat rotation curves ( $\Omega \propto R^{-1}$ ). In a few cases (e.g., NGC 4736 and 5457), large spikes in  $\Sigma_{\text{crit}}$  are seen; these are likely due to errors in determining  $dv_c/dR$  via interpolation.

At first glance, it is impressive how well the relation  $\Sigma_{\text{gas}} \approx \Sigma_{\text{crit}}$  holds for some of the galaxies (NGC 4501, 5033, and 5055). On the other hand, there are two galaxies (NGC 4321 and 4414) where  $\Sigma_{\text{gas}} > \Sigma_{\text{crit}}$  over a significant range of radius, while in NGC 4736 and 5457,  $\Sigma_{\text{gas}} < \Sigma_{\text{crit}}$  across most of the disk. The discrepancies are generally within a factor of 2, which is certainly within the plausible range of error for either  $\Sigma_{\text{gas}}$  (where a constant  $X$ -factor has been used and the CO profile extrapolated) or  $\Sigma_{\text{crit}}$  (which depends on the assumed velocity dispersion, inclination, and distance). Note, however, that the greatest uncertainties are probably associated with the  $X$ -factor and  $c_g$ , and given our choices for these parameters

we have probably *overestimated*  $\Sigma_{\text{gas}}$  and *underestimated*  $\Sigma_{\text{crit}}$ . Thus, the large inferred values for  $Q_g = \Sigma_{\text{crit}}/\Sigma_{\text{gas}}$  are almost certainly significant for NGC 4736 and 5457, yet star formation is hardly suppressed in these galaxies. (Surprisingly, these two galaxies are among those used by Kennicutt to argue for a  $Q$  threshold.)

Indeed, we find no clear evidence that  $\Sigma_{\text{crit}}$  is relevant to  $\Sigma_{\text{SFR}}$  in the inner disk, since in most cases the  $\Sigma_{\text{crit}}$  profile is relatively featureless, a reflection of the relatively featureless rotation curve. For instance, in NGC 4321 it appears to be the case that star formation is enhanced when  $\Sigma_{\text{gas}} > \Sigma_{\text{crit}}$  and vice versa. Yet this may simply be due to the SFR profile roughly tracking the gas density profile (see also Fig. 3). Similarly, the starburst ring in NGC 4736 is associated with an increase in  $\Sigma_{\text{gas}}$ , not a dip in  $\Sigma_{\text{crit}}$ . Thus one should carefully examine claims that star formation occurs in a certain region because the gas density exceeds the critical density. The fact that the gas surface density is higher is probably relevant, but the critical density itself may not be.

While the  $Q$  model was primarily intended to explain the outer disk cutoff of star formation (Kennicutt 1989), our data do not provide strong constraints in this regime. Deep, wide-field H $\alpha$  imaging is required, ideally with spatially resolved measurements of the gas velocity dispersion. Such a study has been undertaken by Ferguson et al. (1998), who found that a threshold radius could not be defined for NGC 6946 when using measured values for  $c_g$  from Kamphuis (1993), although qualitative agreement with the  $Q$  model could be achieved if  $c_g$  were assumed to be constant with radius. Since  $c_g$  is very difficult to measure in galaxies that are not face-on, it is unclear whether this result indicates a failure of the  $Q$  model or reflects inaccuracies in the measurement of  $c_g$ .

#### 4.3. A Relationship Between Atomic and Molecular Gas

The results of §4.1.1, which showed that the SFR traces the radial CO distribution and not the H I, imply that the SFR on large scales will be strongly influenced by the fraction of interstellar matter in molecular form. In a steady-state configuration, this fraction is determined by a balance between molecular cloud formation and destruction processes. The timescales of these processes and the amount of material involved can only be determined empirically when there are organized features, such as spiral arms, with which one can trace the H I/H<sub>2</sub> ratio azimuthally. In the inner disk of M51, for example, virtually all of the H I is believed to result from dissociation of H<sub>2</sub> in the spiral arms (Vogel et al. 1988; Tilanus & Allen 1989; Rand et al. 1992). Conversely, Heyer & Terebey (1998) find that the gas entering the Perseus arm in the outer Galaxy is primarily atomic; in this case the H I must be a precursor to the H<sub>2</sub> in the arm. We will defer discussion of time-dependent processes to a future paper that includes azimuthal comparisons, and will focus instead on what determines the time-averaged H I/H<sub>2</sub> ratio. Thus we ignore the question of whether H I is a product of H<sub>2</sub> or vice versa, since in a time-averaged sense the distinction has little meaning.

In comparing the azimuthally averaged values of  $\Sigma_{\text{HI}}$  and  $\Sigma_{\text{H}_2}$ , we are restricted to a fairly narrow region in the disk:  $R > 20''$ , in order to minimize the effect of beam

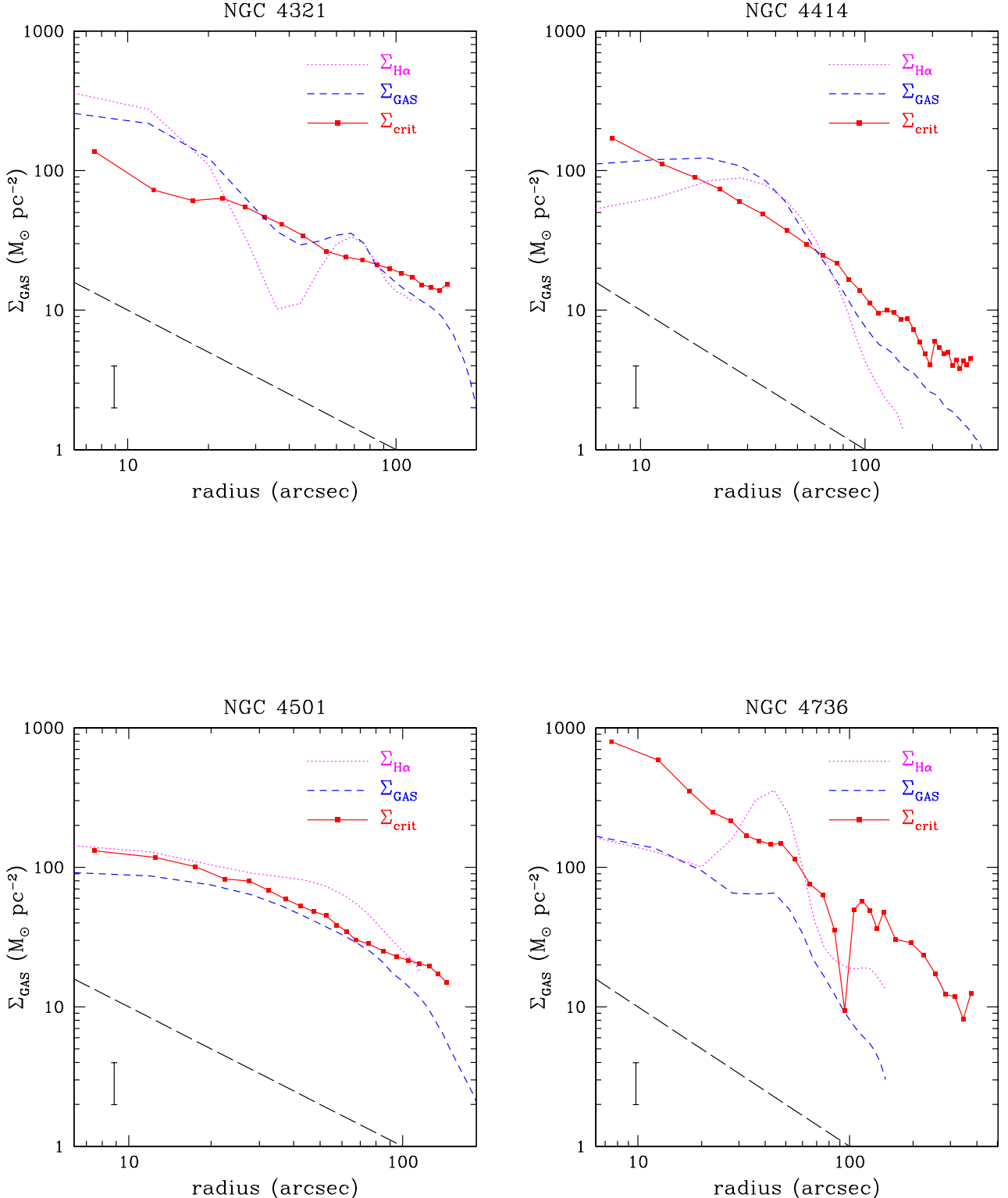


FIG. 11.— Comparison of total gas density with the critical density for gravitational instability for NGC 4321, 4414, 4501, and 4736. The  $\text{H}\alpha$  profile, uncorrected for extinction, is also shown for comparison (dotted line). The error bar at the lower left represents a factor of 2 change, and the heavy dashed line represents an  $R^{-1}$  profile, as expected for  $\Sigma_{\text{crit}}$  with a flat rotation curve.

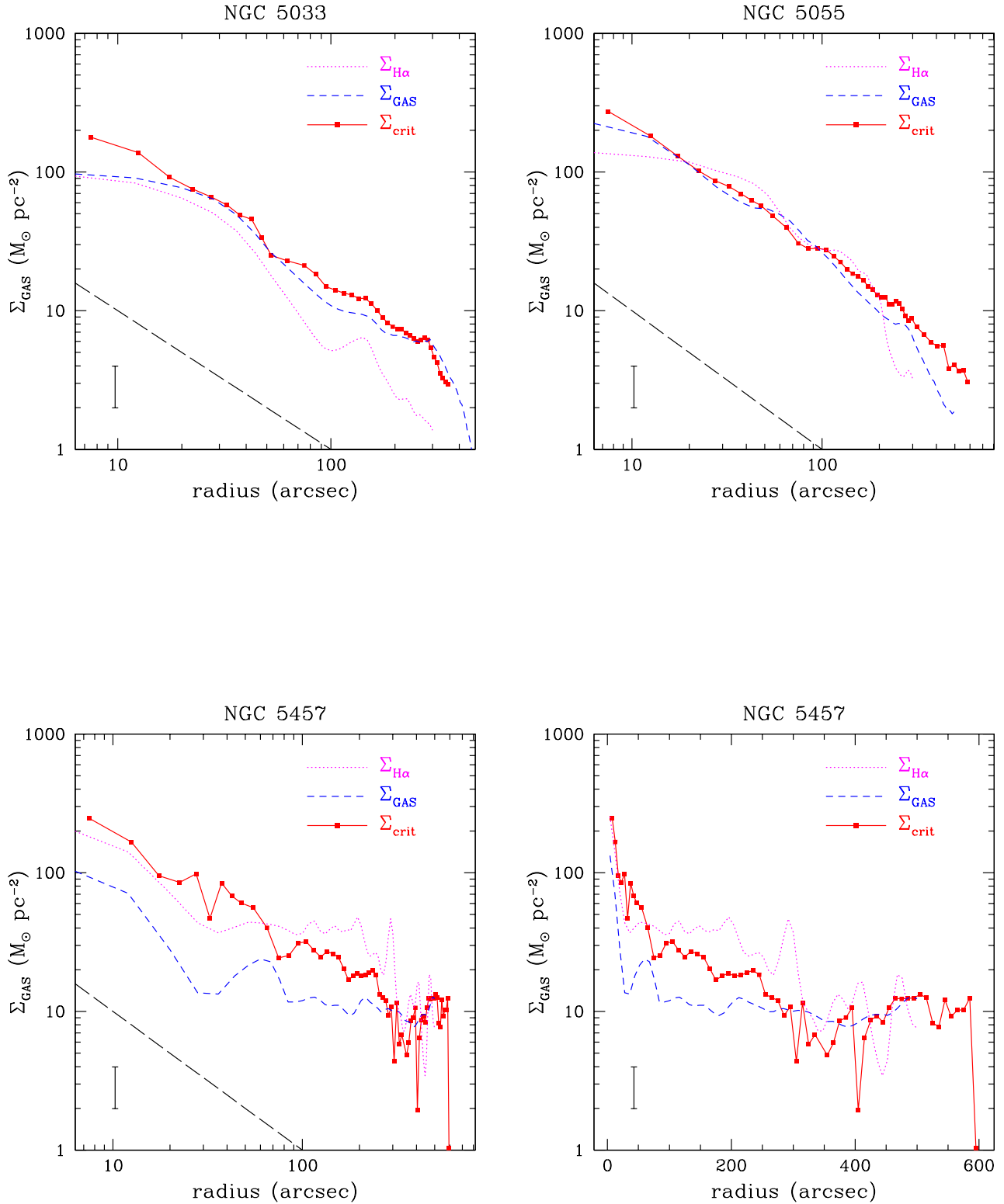


FIG. 12.— Same as Figure 11, for NGC 5033, 5055, and 5457. For NGC 5457 the horizontal axis is also shown on a linear scale (*lower right*).

smearing on the profile, and  $R \lesssim 80''$ , the extent of our CO observations. Furthermore, we have rejected points where  $\Sigma_{\text{HI}} < 1 M_{\odot} \text{ pc}^{-2}$ , because the H I profile is generally uncertain at these radii (this was only an issue for  $R < 36''$  in NGC 5457). In practice, this means that we only probe a region where the molecular fraction  $f_{\text{mol}}$  falls from  $\sim 0.9$ –1 to  $\sim 0.6$ –0.7, emphasizing the need for high sensitivity, large-field CO data to fully analyze the transition region. Figure 13 compares the azimuthally averaged H I and H<sub>2</sub> surface densities for all seven galaxies over the region satisfying the above criteria. The two types of behavior seen in the radial gas profiles in Fig. 3 are reflected in whether  $\Sigma_{\text{HI}}$  is constant with increasing  $\Sigma_{\text{H}_2}$  or begins to decrease at some point. In NGC 4414, 5033, and 5055, the H I profile remains relatively flat across the inner disk, while in NGC 4321, 4501, 4736, and 5457, the H I profile declines toward the center.

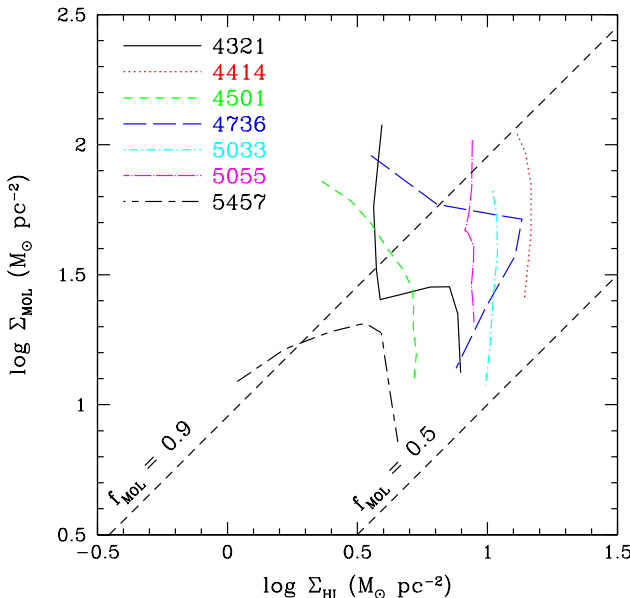


FIG. 13.— Relation between molecular and atomic gas surface density for all seven galaxies in the region where observations overlap ( $R_{\min}=20''$ ,  $R_{\max} \sim 80''$ ) and where  $\Sigma_{\text{HI}} > 1 M_{\odot} \text{ pc}^{-2}$ .

As shown in Figure 14, the ratio of  $\Sigma_{\text{HI}}$  to  $\Sigma_{\text{H}_2}$  appears to depend on radius, increasing as roughly

$$\frac{\Sigma_{\text{HI}}}{\Sigma_{\text{H}_2}} = KR^{1.5} \quad (21)$$

over a factor of  $\sim 2$  (0.3 dex) in  $R$ . The fact that the curves in Fig. 14 are parallel but are spread out over nearly an order of magnitude in  $R$  indicates that there is a second parameter  $K$  that is roughly constant *within* a galaxy but varies from galaxy to galaxy. If  $K$  is taken to be  $(R_{25})^{-1.5}$ , where  $R_{25}$  is the optical radius given in Table 1, then the residual variation in  $\log R$ , although still substantial, is reduced to  $\sim 0.5$  dex. The most striking aspect of the relation given by Equation (21) is that it is independent of whether the H I profile is flat or declining towards the center: note especially how it “straightens out” the lines for NGC 4321, 4736, and 5457 when compared to Fig. 13. Thus, *the ratio of  $\Sigma_{\text{HI}}$  to  $\Sigma_{\text{H}_2}$  appears to depend on galactocentric radius, normalized by  $R_{25}$ , and little else*. In galaxies where the inner H I profile is flat,  $\Sigma_{\text{H}_2}$  declines

as roughly  $R^{-1.5}$ , whereas the galaxies with H I decreasing towards the center have a correspondingly flatter H<sub>2</sub> profile across the transition region. We discuss a possible interpretation of these trends in §5.4.

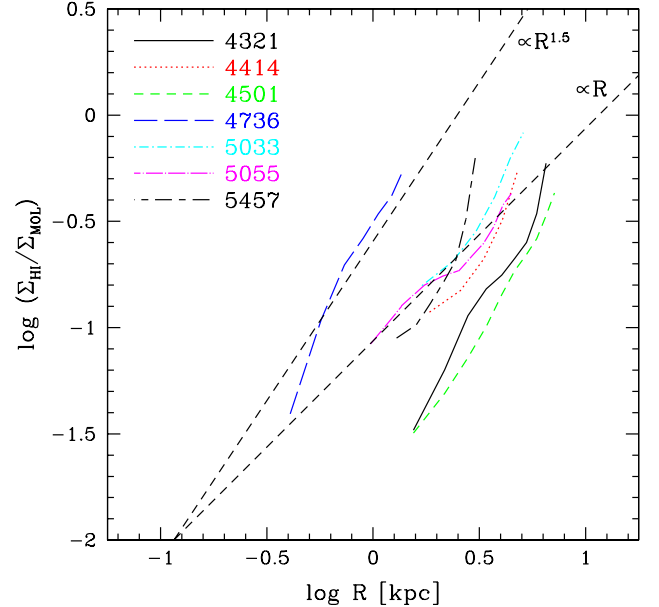


FIG. 14.— Ratio of H I to H<sub>2</sub> surface density plotted against radius for all seven galaxies. Two power-law parameterizations are shown, one where the ratio scales with  $R$  and another where the ratio scales with  $R^{1.5}$ . The data are the same as shown in Figure 13.

## 5. DISCUSSION

### 5.1. Does CO Trace Molecular Mass?

We have interpreted the linearity between azimuthally averaged CO and H $\alpha$  emission (§4.1.1) as indicative of a constant star formation efficiency, but it could conceivably be a result of CO excitation effects. That is, if energy input from young stars is responsible for exciting the CO emission, then CO may trace star formation directly rather than the H<sub>2</sub> mass (e.g., Dopita & Ryder 1994). Evidence in favor of this viewpoint comes from observations of the [C II] 158  $\mu\text{m}$  line, a tracer of photodissociation regions, which is found to scale linearly with the CO(1–0) flux in infrared-luminous galaxies (Crawford et al. 1985). However, relatively stronger CO emission (compared to [C II]) is found in spirals with more typical SFRs (Stacey et al. 1991), and further studies with higher-resolution instruments such as SOFIA will be essential.

In any case, there are at least three difficulties with the suggestion that we have significantly overestimated the H<sub>2</sub> mass in regions of active star formation. First, the gas depletion times are already quite short in these regions,  $\sim 1$ –3 Gyr, and become even shorter if there is less H<sub>2</sub>; it seems unlikely that we would happen to witness the final stages of star formation in these regions. Second, observations of cold dust in nearby galaxies with the SCUBA submillimeter camera show a strong correlation between CO and 850  $\mu\text{m}$  emission (e.g., Alton et al. 2001), indicating that variations in the  $X$ -factor with radius cannot significantly exceed variations in the gas-to-dust ratio. Finally, the spa-

tial correspondence between CO and young massive stars (which would dominate the radiative excitation) does not appear to be close when observations of sufficient angular resolution are performed. Note for instance the different azimuthal symmetries of CO and H $\alpha$  in NGC 4736 (Wong & Blitz 2000), or the spatial offset between the brightest CO emission and the most populous young clusters in the LMC (Cohen et al. 1988).

### 5.2. Interpretation of the Schmidt Law

Previous evidence for a power-law relationship between  $\Sigma_{\text{gas}}$  and  $\Sigma_{\text{SFR}}$ , with  $n \approx 1.5$ , has been discussed by Kennicutt (1997) and K98. As shown in §4.1, this relation appears to hold within galaxies as well. The most straightforward interpretation of such a Schmidt law is that the SFR on large scales is controlled by the self-gravity of the gas. As a result, the rate of star formation is proportional to the gas mass divided by the timescale for gravitational collapse:

$$\rho_{\text{SFR}} = \frac{\epsilon_* \rho_{\text{gas}}}{(G \rho_{\text{gas}})^{-0.5}} \propto \rho_{\text{gas}}^{1.5}. \quad (22)$$

The problem with this explanation, however, is that the efficiency factor  $\epsilon_*$  is observed to be much less than 1. In other words, the gas depletion time on large scales ( $\tau_{\text{gas}} \sim 10^9$  yr), while often much less than a Hubble time, is still significantly longer than  $\tau_{\text{ff}} = (G \rho_{\text{gas}})^{-0.5} \approx 10^7 - 10^8$  yr for  $n_{\text{H}} \sim 1-100$  cm $^{-3}$ . This leads to two competing interpretations: (1) the star formation timescale really is  $\tau_{\text{ff}}$ , but only a small fraction  $\epsilon_*$  of the gas participates in star formation (Elmegreen 2000), or (2) the star formation timescale is  $\tau_{\text{ff}}$  multiplied by a factor of  $\epsilon_*^{-1}$ , due to the inhibiting effects of stellar feedback (i.e., winds, radiation, and supernovae) or magnetic support on star formation (Larson 1988). Neither description, however, offers a clear prediction for the value of  $\epsilon_*$  or explains why it should be constant. Replacing  $\tau_{\text{ff}}$  with the orbital timescale  $\tau_{\text{orb}}$ , as discussed in §4.1.3, yields a similar problem: why is a small but fixed fraction of the gas consumed per orbit?

Given that the theoretical basis of the Schmidt law remains unclear, it is worthwhile to consider an alternative explanation, motivated by our finding in §4.1.1 that  $\Sigma_{\text{SFR}}$  scales roughly linearly with  $\Sigma_{\text{H}_2}$ —a result that is also consistent with previous extragalactic (Rownd & Young 1999) and Galactic (McKee 1989) studies. In this picture, stars form only in molecular gas, and the timescale for star formation is controlled by stellar feedback, magnetic diffusion, or other processes which do not vary strongly with location in a galaxy, so that  $\Sigma_{\text{SFR}} \propto \Sigma_{\text{H}_2}$  ( $n_{\text{mol}}=1$ ). As suggested by Tacconi & Young (1986) and Wang (1990), the Schmidt law between  $\Sigma_{\text{SFR}}$  and the total gas surface density  $\Sigma_{\text{gas}}$  follows from an amalgamation of two “laws,” the first relation governing the formation of  $\text{H}_2$  from H I, and the second (linear) relation governing the formation of stars from  $\text{H}_2$ . The composite Schmidt law index is given by

$$n = \frac{d \ln \Sigma_{\text{SFR}}}{d \ln \Sigma_{\text{gas}}} \quad (23)$$

$$= \left( \frac{d \ln \Sigma_{\text{SFR}}}{d \ln \Sigma_{\text{H}_2}} \right) \left( \frac{d \ln \Sigma_{\text{H}_2}}{d \ln \Sigma_{\text{gas}}} \right) \quad (24)$$

$$= \left( \frac{d \ln \Sigma_{\text{SFR}}}{d \ln \Sigma_{\text{H}_2}} \right) \left( \frac{d \ln \Sigma_{\text{gas}} + d \ln f_{\text{mol}}}{d \ln \Sigma_{\text{gas}}} \right) \quad (25)$$

$$= n_{\text{mol}} \left( 1 + \frac{d \ln f_{\text{mol}}}{d \ln \Sigma_{\text{gas}}} \right). \quad (26)$$

For  $n_{\text{mol}} \approx 1$  and  $f_{\text{mol}}$  increasing with  $\Sigma_{\text{gas}}$  (since  $f_{\text{mol}}$  increases with interstellar pressure which scales with  $\Sigma_{\text{gas}}$ —see §5.4 below), one naturally arrives at  $n \gtrsim 1$ . Physically this also makes more sense than a star formation law based on the *total* gas surface density, since when one looks in the third dimension, one finds that the vertical distribution of star formation corresponds to that of  $\text{H}_2$ , not H I. The sharp increase in the Schmidt law index  $n$  seen at low  $\Sigma_{\text{gas}}$ , which Kennicutt (1989) attributes to a  $Q$ -dependent threshold for star formation, could instead be due to a sudden decrease in  $f_{\text{mol}}$  at low  $\Sigma_{\text{gas}}$  (or low  $\rho_{\text{gas}}$ , if the volume density is more relevant due to flaring of the HI layer, Ferguson et al. 1998), although the two thresholds may turn out to be equivalent if molecular cloud complexes are formed by large-scale gravitational instabilities.

This “two-step” model is not without its difficulties—it still does not predict the SFE in molecular clouds quantitatively, nor does it explain the enhanced SFE’s found in merging galaxies (Young et al. 1996) or starburst rings (Wong & Blitz 2000), which could be related to cloud collisions (e.g., Tan 2000). However, it does provide an attractive explanation for the relatively constant star formation histories of disks (Kennicutt et al. 1994), namely that the requirement of converting H I into  $\text{H}_2$  could limit the SFR at early times, despite a greater supply of gas. Rana & Wilkinson (1986) have presented such a model, in which the  $\text{H}_2$  formation rate at early epochs is limited by the lack of metals, since metals serve as important coolants in the ISM and constitute the dust grains on which most of the  $\text{H}_2$  forms. Even today, the confinement of  $\text{H}_2$  to a thinner disk than the H I (see e.g., studies of NGC 891 by Scoville et al. 1993; Swaters et al. 1997) suggests that the formation of  $\text{H}_2$  is inhibited outside of the midplane, perhaps because of insufficient pressure or dust abundance (see also the discussion in §5.4 below).

### 5.3. Is $Q$ Relevant to Star Formation?

We have found that the  $Q_g$  parameter, defined using a constant velocity dispersion of 6 km s $^{-1}$ , appears to be remarkably close to 1 in some galaxies, but is significantly greater than 1 in NGC 4736 and 5457, which are still actively forming stars. Our observations thus lend support to earlier studies which have failed to show a clear relationship between  $Q_g$  and the presence of massive star formation (Thornley & Wilson 1995; Meurer et al. 1996; Ferguson et al. 1998; Hunter et al. 1998; Pisano et al. 2000). This is not altogether surprising; Elmegreen (1999) raises the question of “why  $Q < 1$  has anything at all to do with star formation in a supersonically turbulent medium filled with supernovae, magnetic fields, multiple gas phases and other seemingly important details.” Yet the problem remains of explaining why  $Q_g \sim 1$  is often observed in galaxy disks, a fact that has long been taken to indicate that star formation on large scales is regulated by gravitational instability (Quirk 1972; Kennicutt 1989; Silk 1997). A possible clue is that  $Q_g$  is significantly greater than 1 in the two galaxies with the lowest gas fractions (NGC 4736 and 5457), as inferred from a comparison of  $\Sigma_{\text{gas}}$  with the stellar surface

density  $\Sigma_*$  derived by assuming a maximum disk (see Paper II). This suggests that  $Q_g$  is actually a measure of the gas fraction in the disk.

A simplified analysis suggests that this is indeed the case. For a Mestel (1963) disk, with  $\Sigma_{\text{tot}} \propto R^{-1}$ , a flat rotation curve is obtained such that

$$v_c^2 = 2\pi G \Sigma_{\text{tot}} R, \quad (27)$$

$$\Sigma_{\text{tot}} = \frac{v_c \Omega}{2\pi G}. \quad (28)$$

[See Binney & Tremaine (1987), p. 76.] But for a flat rotation curve, the critical density is given by

$$\Sigma_{\text{crit}} = \frac{\sqrt{2}\Omega c_g}{\pi G}. \quad (29)$$

Defining the gas fraction as  $\mu = \Sigma_{\text{gas}}/\Sigma_{\text{tot}}$ , we have

$$\mu Q_g = \frac{\Sigma_{\text{crit}}}{\Sigma_{\text{tot}}} = \frac{2\sqrt{2}c_g}{v_c}, \quad (30)$$

$$Q_g \approx \frac{2.8c_g}{v_c \mu}. \quad (31)$$

Substituting typical values for spiral galaxies ( $c_g=6 \text{ km s}^{-1}$ ,  $v_c=200 \text{ km s}^{-1}$ , and  $\mu=0.1$ ) we find that  $Q=0.84$ . Thus, *the fact that  $Q_g$  is of order unity in many spiral galaxies reflects the fact that the present-day gas fraction is roughly 0.1*. Note that we have implicitly assumed a maximum disk model with negligible bulge or halo, but this analysis will be roughly appropriate if  $\Sigma_{\text{tot}}$  is considered to be whatever mass distribution dominates the rotation curve. For instance, dwarf galaxies exhibit large  $Q_g$  values (e.g., Meurer et al. 1996; van Zee et al. 1997) because they rotate slowly and have gas surface densities that are small compared to the dark matter surface density. We therefore propose that  $Q_g \sim 1$  is primarily a reflection of observational selection favoring luminous, gas-rich galaxies for this kind of analysis; galaxies with smaller gas fractions should show  $Q_g > 1$ . We note that this explains the larger  $Q_g$  values found in early-type galaxies by Martin & Kennicutt (2001). Still, the lack of galaxies with  $Q_g \ll 1$  suggests that *strongly unstable* gas disks are precluded.

That the  $Q_g$  parameter is most sensitive to the gas fraction and thus cannot be the same for all galaxies was recognized many years ago by Larson (1988). He suggested that an increase in  $c_g$  would partially offset the larger  $\Sigma_{\text{gas}}$  at early times, maintaining  $Q_g \sim 1$ . It is unlikely, however, that the velocity dispersion of the gas, when averaged over large scales, can continue to decrease much below a value of  $\sim 6 \text{ km s}^{-1}$ , since measurements in the face-on galaxy NGC 1058 indicate that it does not fall below this value even well beyond the optical radius (van der Kruit & Shostak 1984; Dickey et al. 1990). Sellwood & Balbus (1999) attribute this minimum velocity dispersion to magnetohydrodynamic turbulence that is ultimately fed by the galaxy's differential rotation. Based on these arguments, a secular increase in  $Q_g$  seems inevitable as gas consumption continues, unless new gas is constantly accreted to maintain  $\mu$  at a constant level.

In spite of the apparent difficulties in using  $Q_g$  as a predictor of star formation activity, it is still remarkable how well  $Q_g \approx 1$  is satisfied in certain galaxies, such as NGC 5033 and 5055 (Fig. 12). A possible explanation is that gravitational instability *does* regulate star formation,

but the appropriate  $Q$  parameter must take into account both the gas and stellar disks. Elmegreen (1995) and Jog (1996), extending the work of Jog & Solomon (1984), have shown that the gravitational interaction of these two components leads to greater instability in the combined system than in either component individually. They derive an "effective"  $Q$  parameter  $Q_{\text{eff}}$  which is  $\approx Q_g$  for gas-dominated disks, but can be close to  $Q_*$  when the gas fraction is small. For  $Q_*$  to be regulated at a value of  $\sim 1$  requires only that the stellar velocity dispersion  $c_*$  increase in proportion to the stellar surface density, and is in good agreement with observations if one assumes a constant  $M/L$  ratio in the disk (Bottema 1993). Thus, even galaxies with low gas fractions may be susceptible to mild gravitational instabilities as a result of  $Q_* \sim 1$ , and gravitational instability may be able to account for the presence of continued star formation in these galaxies after all.

As noted by Skillman (1996), an alternative to a  $Q$ -based star formation threshold is a constant column density threshold of  $N_{\text{H}} \sim 10^{21} \text{ cm}^{-2}$  associated with the formation of molecular clouds. In this picture, star formation cuts off at a radius where there is insufficient self-shielding from UV radiation to allow molecular clouds to form. In practice, the column density threshold may vary with metallicity, pressure, and the interstellar radiation field, all of which affect the transition from H I to H<sub>2</sub> (Elmegreen 1993). A similar criterion, in which the minimum column density is defined by the requirement of sufficient pressure to allow a two-phase ISM, has been discussed by Elmegreen & Parravano (1994). Supporting this hypothesis, Braun (1997) has presented evidence that cold H I clouds are not observed outside the optical radius of galaxies; the inability to form such clouds may be responsible for star formation thresholds. A comparison of sensitive CO, H I, and H $\alpha$  data near the edges of galaxy disks would be needed to test these ideas.

#### 5.4. The Atomic-to-Molecular Gas Ratio

In §4.3 we found that the ratio of  $\Sigma_{\text{HI}}$  to  $\Sigma_{\text{H}_2}$  varies within galaxies as roughly  $R^{1.5}$  in the region of overlap. However, the interpretation of this dependence is ambiguous, since many galaxy properties vary with radius. Moreover, the limited range in radius over which the ratio is calculated may allow for a variety of functional forms, of which this relation is only the simplest. For purposes of discussion, we consider here two possible models for how  $\Sigma_{\text{HI}}$  and  $\Sigma_{\text{H}_2}$  should be related, and compare them with our results.

First, Wyse (1986) has suggested that the formation of GMCs is tied to collisions between atomic clouds as they pass through spiral arms. Assuming a negligible pattern speed (i.e., well inside the corotation radius), the rate of spiral arm crossings at radius  $R$  is  $\propto \Omega(R)$ , and one expects

$$\Sigma_{\text{H}_2} \propto (\Sigma_{\text{HI}})^2 \Omega. \quad (32)$$

This naturally introduces an  $R$  dependence into the ratio  $\Sigma_{\text{HI}}/\Sigma_{\text{H}_2}$ , qualitatively similar to the  $R^{1.5}$  dependence we derived above. However, Figure 15 shows that while the majority of the galaxies show *some* correlation between  $\Sigma_{\text{H}_2}$  and  $(\Sigma_{\text{HI}})^2 \Omega$ , the expected relation (given by the dashed line) is a much poorer description of the data than the simple  $R^{1.5}$  relation shown in Fig. 14.

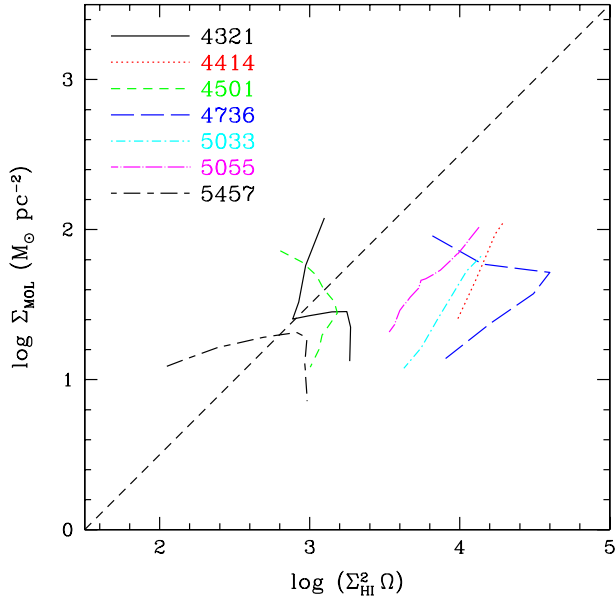


FIG. 15.— Surface density of molecular gas vs. the prediction from Wyse (1986), where  $\Sigma_{\text{H}_2} \propto \Sigma_{\text{HI}}^2 \Omega$ . The dashed line represents a slope of 1, in agreement with the prediction.

Second, Elmegreen (1993) argues that the degree to which a cloud is molecular is determined in part by the ambient pressure  $P$ , since the molecule formation rate depends on the volume density  $n$ , which scales with  $P$  for both diffuse and self-gravitating clouds. The pressure at the midplane of a two-component disk in hydrostatic equilibrium is given by (Elmegreen 1989):

$$P \approx \frac{\pi}{2} G \Sigma_{\text{gas}} \left( \Sigma_{\text{gas}} + \frac{c_g}{c_*} \Sigma_* \right), \quad (33)$$

where  $c_g$  and  $c_*$  are the velocity dispersions of the gaseous and stellar disk respectively. The observations of Bottema (1993) typically give  $c_* \sim 60 \text{ km s}^{-1}$ , so we assume a value for  $c_g/c_*$  of 0.1. (This value for  $c_*$  is consistent with the velocity dispersion of an isothermal disk,  $c_* = \sqrt{\pi G \Sigma_* z_0}$ , for  $\Sigma_* \sim 300 \text{ M}_\odot \text{ pc}^{-2}$  and  $z_0 \sim 1 \text{ kpc}$ .) We have derived radial profiles of  $\Sigma_*$  using  $K$  or  $I$ -band profiles with a mass-to-light ( $M/L$ ) ratio chosen to provide a maximal disk contribution to the rotation curve, as discussed further in Paper II. As shown in Figure 16(a), a relation of the form

$$\Sigma_{\text{HI}}/\Sigma_{\text{H}_2} \propto P^{-0.8} \quad (34)$$

appears to match the data reasonably well. For comparison, Elmegreen (1993) predicts a very sensitive dependence of the molecular fraction  $f_{\text{mol}}$  on pressure:  $f_{\text{mol}} \propto P^{2.2} j^{-1}$ , where  $j$  is the volume emissivity of dissociating radiation. For  $j \propto \Sigma_* \propto \Sigma_{\text{gas}}$ , this leads to  $f_{\text{mol}} \propto P^{1.7}$ , which is clearly steeper than what is observed within our galaxies [Fig. 16(b)]. However, his parametrization is intended for use in the low  $f_{\text{mol}}$  regime, which is more appropriate for the Milky Way than for  $\text{H}_2$ -dominated galaxies; indeed the match to the Galactic data of Dame (1993) is reasonably good [Fig. 16(b)].

Residual offsets between galaxies in Fig. 16(a) may result from uncertainties in the adopted  $M/L$  ratio, or could be related to additional physical parameters, such as metallicity. Specifically, we find that galaxies with oxygen abundances significantly above solar in their inner ( $R < 200''$ ) disks (NGC 4321, 4501, 5055, and 5457)

display smaller values of  $\Sigma_{\text{HI}}/\Sigma_{\text{H}_2}$ . Higher metallicity is expected to favor the formation of  $\text{H}_2$ , since dust attenuates the dissociating UV radiation field and provides a surface on which to form  $\text{H}_2$ . The importance of metallicity in the  $\text{H I-H}_2$  balance is discussed further by Rana & Wilkinson (1986) and Honma et al. (1995). However, we caution that the use of CO to trace  $\text{H}_2$  may also introduce a metallicity dependence in our derived value of  $\Sigma_{\text{HI}}/\Sigma_{\text{H}_2}$ .

Thus, while the range in  $f_{\text{mol}}$  probed by our observations is fairly small, the trend in the  $\text{H I}/\text{H}_2$  ratio with radius suggests that pressure is playing the dominant role, with metallicity as a secondary factor. This is supported by observations indicating that the global  $M_{\text{HI}}/M_{\text{H}_2}$  ratio increases from early-type to late-type galaxies (Young & Knezek 1989; Casoli et al. 1998), since early-type galaxies generally have higher mass surface densities (and metallicities). Moreover, the tendency for recent star formation to be correlated with the distribution of stellar light, noted for example by Ryder & Dopita (1994) and Hunter et al. (1998), can be explained if stars currently dominate the pressure which controls  $\text{H}_2$  and star formation. Further observations spanning a wider range of  $f_{\text{mol}}$  would be useful to verify the importance of pressure in determining the  $\text{H I}/\text{H}_2$  balance.

## 6. SUMMARY AND CONCLUSIONS

We have investigated the relationship between gas content and star formation rate, commonly termed the star formation law, in seven nearby galaxies using CO, HI, and  $\text{H}\alpha$  images at resolutions of  $\sim 20''$  or higher. An important advance is the recent availability of CO data that combines the resolution of an interferometer with the sensitivity to large-scale structure afforded by a single-dish telescope. Although our sample is biased toward luminous, molecule-rich galaxies, none of the galaxies display signs of strong interactions.

We find that the correlation of the azimuthally averaged SFR surface density  $\Sigma_{\text{SFR}}$  with  $\Sigma_{\text{HI}}$  is much poorer than with  $\Sigma_{\text{H}_2}$ , contrary to the results of studies based on integrated fluxes. Whereas a roughly linear relation exists between  $\Sigma_{\text{SFR}}$  and  $\Sigma_{\text{H}_2}$ , consistent with a constant star formation efficiency for the molecular gas,  $\Sigma_{\text{HI}}$  tends to reach a maximum value of  $\sim 10 \text{ M}_\odot \text{ pc}^{-2}$ , or even decline in regions of high SFR. Thus the star-forming gas in these galaxies exists predominantly in molecular form, although the situation may be different in low-mass galaxies.

Despite the poor correlation of  $\Sigma_{\text{SFR}}$  with  $\Sigma_{\text{HI}}$ , the dominance of  $\text{H}_2$  in these galaxies leads to a strong correlation between  $\Sigma_{\text{SFR}}$  and total gas surface density  $\Sigma_{\text{gas}}$  when azimuthally averaged, in rough agreement with the global Schmidt law derived by K98. The index of the power law is given by  $n \approx 1.1$  if the extinction at  $\text{H}\alpha$  is assumed to be uniform with radius, but steepens to  $n \approx 1.7$  if the mean extinction is assumed to vary according to the gas surface density. A star formation law of the form  $\Sigma_{\text{SFR}} \propto \Sigma_{\text{gas}} \Omega$  is also consistent with the data, but only if the  $N_{\text{H}}$ -dependent extinction corrections are applied. We suggest that the observed Schmidt law results from an effective dependence of the molecular fraction on  $\Sigma_{\text{gas}}$  by way of the interstellar pressure, coupled with a roughly linear relation between  $\Sigma_{\text{SFR}}$  and  $\Sigma_{\text{H}_2}$ .

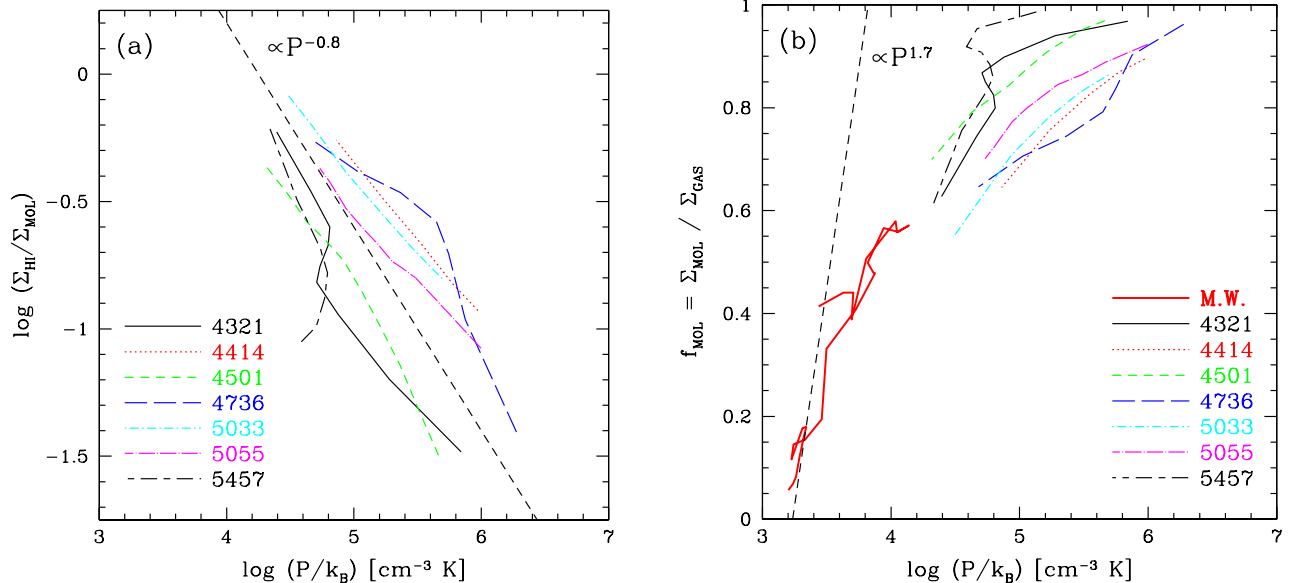


FIG. 16.— (a) Ratio of H I to H<sub>2</sub> surface density plotted against the hydrostatic disk pressure at the midplane, as given by Elmegreen (1989). The straight dashed line represents the mean slope of  $-0.8$ . (b) Molecular fraction plotted against midplane pressure. The straight dashed line represents the slope of  $1.7$  predicted by Elmegreen (1993). Data for the Milky Way is based on Dame et al. (1993), adopted a stellar scalelength of  $3$  kpc (Sackett 1997) and  $\Sigma_{*} = 35 M_{\odot} \text{ pc}^{-2}$  at the solar circle (Gilmore et al. 1989).

The gravitational instability parameter  $Q_g$  is found to be  $\sim 1$  in several galaxies but is clearly  $> 1$  in the two galaxies with the smallest gas fractions, NGC 4736 and 5457. We suggest that  $Q_g$  is best considered a measure of the gas fraction, and that when discussing a range of galaxy types, the contribution of the stellar component to the disk instability should not be neglected. While a combined (gaseous and stellar) instability may ultimately provide a better description of star formation thresholds, alternative explanations that attribute such thresholds to the inability to form cold, dense clouds remain attractive as well.

Finally, over the limited range in radius where our CO and H I data overlap, we find that the relation  $\Sigma_{\text{HI}}/\Sigma_{\text{H}_2} \propto R^{1.5}$  holds remarkably well within galaxies, although the proportionality constant varies among galaxies. We show that such a relation supports the view that the interstellar pressure plays the dominant role in determining the H I-H<sub>2</sub> balance.

These results have demonstrated the importance of including the molecular component in studying the star formation law. Moreover, considering just the total gas density rather than the H I and H<sub>2</sub> surface densities separately may obscure underlying physical processes that are essential to star formation. In a future study, we will develop these ideas using the much larger CO database provided by the BIMA SONG project, supplemented by archival and recently obtained H I synthesis imaging. We also em-

phasize that significant advances will be made possible by improved measurements of extinction within galaxies to enable more accurate estimates of the SFR, and by studies of the vertical structure of edge-on galaxies, which will provide further insight into the H I-H<sub>2</sub> transition and its relationship to the ISM pressure.

We thank our collaborators on BIMA SONG, particularly D. Bock, T. Helper, M. Regan, K. Sheth, M. Thornley, and S. Vogel, for their role in conducting many of the observations used in this study, and for extensive discussions and suggestions. C. McKee provided useful comments to an earlier draft of this paper, and suggested a more careful treatment of extinction. Constructive comments by W. J. G. de Blok, B. Elmegreen, S. Ryder, and the referee, C. Wilson, are also appreciated. We are indebted to A. Bosma, R. Braun, V. Cayatte, R. Kennicutt, J. Knapen, C. Mundell, A. Thean, J. van Gorkom, and L. van Zee for providing us with data for this study. This research is based on the Ph.D. thesis of T.W. and has been supported by National Science Foundation grants AST 96-13998 and 99-81308 to the U.C. Berkeley Radio Astronomy Laboratory, and a Bolton Fellowship from the Australia Telescope National Facility. Finally, this project would have been much more difficult without the convenience provided by NASA's Astrophysics Data System (ADS) Abstract Service and the NASA/IPAC Extragalactic Database (NED), which is gratefully acknowledged.

## REFERENCES

Akeson, R. L. 1998, BIMA Memorandum No. 68  
 Alton, P. B., Lequeux, J., Bianchi, S., Churches, D., Davies, J., & Combes, F. 2001, A&A, 366, 451  
 Beckman, J. E., Rozas, M., Zurita, A., Watson, R. A., & Knapen, J. H. 2000, AJ, 119, 2728  
 Bell, E. F. & Kennicutt, R. C. 2001, ApJ, 548, 681  
 Belley, J. & Roy, J.-R. 1992, ApJS, 78, 61  
 Binney, J. & Tremaine, S. 1987, Galactic Dynamics (Princeton: Princeton U. Press)  
 Bohlin, R. C., Savage, B. D., & Drake, J. F. 1978, ApJ, 224, 132  
 Boissier, S. & Prantzos, N. 1999, MNRAS, 307, 857  
 Boselli, A. 1994, A&A, 292, 1  
 Bosma, A. 1981, AJ, 86, 1791  
 Bottema, R. 1993, A&A, 275, 16  
 Braun, R. 1995, A&AS, 114, 409

—. 1997, *ApJ*, 484, 637

Buat, V., Deharveng, J. M., & Donas, J. 1989, *A&A*, 223, 42

Casoli, F., Dickey, J., Kazès, I., Boselli, A., Gavazzi, P., & Baumgardt, K. 1996, *A&A*, 309, 43

Casoli, F., Sauty, S., Gerin, M., Boselli, A., Fouqué, P., Braine, J., Gavazzi, G., Lequeux, J., & Dickey, J. 1998, *A&A*, 331, 451

Cohen, R. S., Dame, T. M., Garay, G., Montani, J., Rubio, M., & Thaddeus, P. 1988, *ApJ*, 331, L95

Combes, F. & Bercquaert, J.-F. 1997, *A&A*, 326, 554

Condon, J. J. 1992, *ARA&A*, 30, 575

Crawford, M. K., Genzel, R., Townes, C. H., & Watson, D. M. 1985, *ApJ*, 291, 755

Dahmen, G., Hüttemeister, S., Wilson, T. L., & Mauersberger, R. 1998, *A&A*, 331, 959

Dame, T. 1993, in *Back to the Galaxy*, ed. S. Holt & F. Verter (New York: AIP), 267

Dame, T. M., Hartmann, D., & Thaddeus, P. 2001, *ApJ*, 547, 792

Dame, T. M., Koper, E., Israel, F. P., & Thaddeus, P. 1993, *ApJ*, 418, 730

de Vaucouleurs, G., de Vaucouleurs, A., Corwin, H. G., Buta, R. J., Paturel, G., & Fouqué, P. 1991, *Third Reference Catalogue of Bright Galaxies* (New York: Springer-Verlag)

Deharveng, J.-M., Sasasseen, T. P., Buat, V., Bowyer, S., Lampton, M., & Wu, X. 1994, *A&A*, 289, 715

Devereux, N. A. & Young, J. S. 1991, *ApJ*, 371, 515

Dickey, J. M., Hanson, M. M., & Helou, G. 1990, *ApJ*, 352, 522

Dickey, J. M. & Lockman, F. J. 1990, *ARA&A*, 28, 215

Dopita, M. A. & Ryder, S. D. 1994, *ApJ*, 430, 163

Dove, J. B. & Shull, J. M. 1994, *ApJ*, 430, 222

Elmegreen, B. G. 1989, *ApJ*, 338, 178

—. 1993, *ApJ*, 411, 170

—. 1995, *MNRAS*, 275, 944

Elmegreen, B. G. 1999, in *Star Formation 1999*, ed. T. Nakamoto (Nobeyama Radio Observatory), 3

—. 2000, *ApJ*, 530, 277

Elmegreen, B. G. & Parravano, A. 1994, *ApJ*, 435, L121

Federman, S. R., Glassgold, A. E., & Kwan, J. 1979, *ApJ*, 227, 466

Ferguson, A. M. N., Wyse, R. F. G., Gallagher, J. S., & Hunter, D. A. 1996, *AJ*, 111, 2265

—. 1998, *ApJ*, 506, L19

Ferrarese, L. et al. 1996, *ApJ*, 464, 568

Gilmore, G., Wyse, R. F. G., & Kuijken, K. 1989, in *Evolutionary Phenomena in Galaxies*, ed. J. Beckman & B. Pagel (Cambridge: Cambridge U. Press), 172

Gooch, R. E. 1995, in *Astronomical Data Analysis Software and Systems V*, ASP Conf. Series Vol. 101, ed. G. H. Jacoby & J. Barnes (San Francisco: ASP), 80

Heyer, M. H. & Terebey, S. 1998, *ApJ*, 502, 265

Honma, M., Sofue, Y., & Arimoto, N. 1995, *A&A*, 304, 1

Hunter, D. A., Elmegreen, B. G., & Baker, A. L. 1998, *ApJ*, 493, 595

Hyman, S. D., Lacey, C. K., Weiler, K. W., & van Dyk, S. D. 2000, *AJ*, 119, 1711

Jog, C. J. 1996, *MNRAS*, 278, 209

Jog, C. J. & Solomon, P. M. 1984, *ApJ*, 276, 114

Kamphuis, J. J. 1993, PhD thesis, Univ. of Groningen

Kelson, D. D. et al. 1996, *ApJ*, 463, 26

Kenney, J. D. P., Scoville, N. Z., & Wilson, C. D. 1991, *ApJ*, 366, 432

Kennicutt, R. C. 1983, *ApJ*, 272, 54

—. 1988, *ApJ*, 334, 144

—. 1989, *ApJ*, 344, 685

—. 1992, *ApJ*, 388, 310

Kennicutt, R. C. 1997, in *The Interstellar Medium in Galaxies*, ed. J. M. van der Hulst (Dordrecht: Kluwer), 171

—. 1998a, *ApJ*, 498, 541

—. 1998b, *ARA&A*, 36, 189

Kennicutt, R. C. & Kent, S. M. 1983, *AJ*, 88, 1094

Kennicutt, R. C., Tamblyn, P., & Congdon, C. W. 1994, *ApJ*, 435, 22

Knapen, J. H., Cepa, J., Beckman, J. E., del Rio, M. S., & Pedlar, A. 1993, *ApJ*, 416, 563

Kotilainen, J. K., Reunanen, J., Laine, S., & Ryder, S. D. 2000, *A&A*, 353, 834

Krabbe, A., Sternberg, A., & Genzel, R. 1994, *ApJ*, 425, 72

Kutner, M. L. & Ulich, B. L. 1981, *ApJ*, 250, 341

Larson, R. 1988, in *Galactic and Extragalactic Star Formation*, ed. R. E. Pudritz & M. Fich (Dordrecht: Kluwer), 459

Lay, O. P. 1999, BIMA Memorandum No. 72

Lequeux, J., Maucherat-Joubert, M., Deharveng, J. M., & Kunth, D. 1981, *A&A*, 103, 305

Loren, R. B., Vanden Bout, P. A., & Davis, J. H. 1973, *ApJ*, 185, L67

Martin, C. L. & Kennicutt, R. C. 2001, *ApJ*, 555, 301

Massey, P., Strobel, K., Barnes, J. V., & Anderson, E. 1988, *ApJ*, 328, 315

Mathis, J. S. 1986, *PASP*, 98, 995

McKee, C. F. 1989, *ApJ*, 345, 782

McKee, C. F. & Williams, J. P. 1997, *ApJ*, 476, 144

Mead, K. N., Kutner, M. L., & Evans, N. J. 1990, *ApJ*, 354, 492

Meier, D. S. & Turner, J. L. 2001, *ApJ*, 551, 687

Mestel, L. 1963, *MNRAS*, 126, 553

Meurer, G. R., Carignan, C., Beaulieu, S. F., & Freeman, K. C. 1996, *AJ*, 111, 1551

Morris, M. & Lo, K. Y. 1978, *ApJ*, 223, 803

Niklas, S., Klein, U., Braine, J., & Wielebinski, R. 1995, *A&AS*, 114, 21

Niklas, S., Klein, U., & Wielebinski, R. 1997, *A&A*, 322, 19

Pisano, D. J., Wilcots, E. M., & Elmegreen, B. G. 2000, *AJ*, 120, 763

Quillen, A. C. & Yukita, M. 2001, *AJ*, 121, 2095

Quirk, W. J. 1972, *ApJ*, 176, L9

Rana, N. C. & Wilkinson, D. A. 1986, *MNRAS*, 218, 497

Rand, R. J., Kulkarni, S. R., & Rice, W. 1992, *ApJ*, 390, 66

Regan, M. W., Thornley, M. D., Helfer, T. T., Sheth, K., Wong, T., Vogel, S. N., Blitz, L., & Bock, D. C.-J. 2001, *ApJ*, in press

Rieke, G. H. & Lebofsky, M. J. 1985, *ApJ*, 288, 618

Rownd, B. K. & Young, J. S. 1999, *AJ*, 118, 670

Rubin, V. C. & Ford, W. K. 1986, *ApJ*, 305, L35

Ryder, S. D. & Dopita, M. A. 1994, *ApJ*, 430, 142

Sackett, P. D. 1997, *ApJ*, 483, 103

Safranov, V. S. 1960, *Ann. d'Ap.*, 23, 979

Sakamoto, K., Okumura, S. K., Ishizuki, S., & Scoville, N. Z. 1999, *ApJS*, 124, 403

Schlegel, D. J., Finkbeiner, D. P., & Davis, M. 1998, *ApJ*, 500, 525

Schmidt, M. 1959, *ApJ*, 129, 243

Scoville, N. Z., Thakkar, D., Carlstrom, J. E., & Sargent, A. I. 1993, *ApJ*, 404, L59

Sellwood, J. A. & Balbus, S. A. 1999, *ApJ*, 511, 660

Shaya, E. J. & Federman, S. R. 1987, *ApJ*, 319, 76

Silk, J. 1997, *ApJ*, 481, 703

Skillman, E. D. 1996, in *The Minnesota Lectures on Extragalactic Neutral Hydrogen*, ASP Conference Series Vol. 106, ed. E. D. Skillman (San Francisco: ASP), 208

Smith, B. J., Lester, D. F., Harvey, P. M., & Pogge, R. W. 1991, *ApJ*, 373, 66

Sodroski, T. J. et al. 1995, *ApJ*, 452, 262

Stacey, G. J., Geis, N., Genzel, R., Lugten, J. B., Poglitsch, A., Sternberg, A., & Townes, C. H. 1991, *ApJ*, 373, 423

Steer, D. G., Dewdney, P. E., & Ito, M. R. 1984, *A&A*, 137, 159

Strong, A. W. & Mattox, J. R. 1996, *A&A*, 308, L21

Swaters, R. A., Sancisi, R., & van der Hulst, J. M. 1997, *ApJ*, 491, 140

Tacconi, L. J. & Young, J. S. 1986, *ApJ*, 308, 600

Tan, J. C. 2000, *ApJ*, 536, 173

Tan, J. C., Silk, J., & Balland, C. 1999, *ApJ*, 522, 579

Taylor, C. L., Kobulnicky, H. A., & Skillman, E. D. 1998, *AJ*, 116, 2746

Thean, A. H. C., Mundell, C. G., Pedlar, A., & Nicholson, R. A. 1997, *MNRAS*, 290, 15

Thornley, M. D. & Mundy, L. G. 1997a, *ApJ*, 484, 202

—. 1997b, *ApJ*, 490, 682

Thornley, M. D. & Wilson, C. D. 1995, *ApJ*, 447, 616

Tilanus, R. P. J. & Allen, R. J. 1989, *ApJ*, 339, L57

Toomre, A. 1964, *ApJ*, 139, 1217

Turner, A. et al. 1998, *ApJ*, 505, 207

van den Bosch, F. C. & Dalcanton, J. J. 2000, *ApJ*, 534, 146

van der Hulst, J. M., Kennicutt, R. C., Crane, P. C., & Rots, A. H. 1988, *A&A*, 195, 38

van der Kruit, P. C. 1990, in *The Milky Way as a Galaxy*, ed. R. Buser & I. R. King (Mill Valley, CA: University Science Books), 331

van der Kruit, P. C. & Shostak, G. S. 1982, *A&A*, 105, 351

—. 1984, *A&A*, 134, 258

van Zee, L., Haynes, M. P., Salzer, J. J., & Broeils, A. H. 1997, *AJ*, 113, 1618

van Zee, L., Salzer, J. J., Haynes, M. P., O'Donoghue, A. A., & Balonek, T. J. 1998, *AJ*, 116, 2805

Vogel, S. N., Kulkarni, S. R., & Scoville, N. Z. 1988, *Nature*, 334, 402

Wang, Z. 1990, *ApJ*, 360, 529

Willick, J. A., Courteau, S., Faber, S. M., Burstein, D., Dekel, A., & Strauss, M. A. 1997, *ApJS*, 109, 333

Wilson, C. D. 1995, *ApJ*, 448, L97

Wong, T. 2000, PhD thesis, Univ. of California at Berkeley

Wong, T. & Blitz, L. 2000, *ApJ*, 540, 771

Wouterloot, J. G. A., Brand, J., & Henkel, C. 1988, *A&A*, 191, 323

Wright, M. C. H. 1996, *PASP*, 108, 520

Wyse, R. F. G. 1986, *ApJ*, 311, L41

Wyse, R. F. G. & Silk, J. 1989, *ApJ*, 339, 700

Young, J. S., Allen, L., Kenney, J. D. P., Lesser, A., & Rownd, B. 1996, *AJ*, 112, 1903

Young, J. S. & Knezek, P. M. 1989, *ApJ*, 347, L55

Young, J. S. et al. 1995, *ApJS*, 98, 219